Convection-allowing and convection-parameterizing ensemble forecasts of a mesoscale convective vortex and associated severe weather environment

Adam J. Clark[1], William A. Gallus Jr.[1], Ming Xue[2,3] and Fanyou Kong[3]

[1] *Department of Geological and Atmospheric Sciences*
Iowa State University
Ames, IA, 50010

[2] *School of Meteorology, and* [3]*Center for Analysis and Prediction of Storms*
University of Oklahoma
Norman, Oklahoma, 73072

Revised manuscript submitted to
Weather and Forecasting
January 2010

* Corresponding author's address:
Adam J. Clark
National Weather Center, NSSL/FRDD
120 David L. Boren Blvd.,
Norman, OK, 73072
email: adam.clark@noaa.gov
Phone: 405-325-6731

Abstract

An analysis of a regional severe weather outbreak that was related to a mesoscale convective vortex (MCV) is performed. The MCV-spawning MCS formed in northwest Kansas along the southern periphery of a large cut-off 500-hPa low centered over western South Dakota. As the MCS propagated into eastern Kansas during the early morning of 1 June 2007, an MCV that became evident from multiple data sources (e.g., WSR-88D radar network, visible satellite imagery, wind-profiler data, Rapid Update Cycle 1-hourly analyses) tracked through northwest Missouri and central Iowa manifest as a well defined mid-level short wave trough. Downstream of the MCV in southeast Iowa and northwest Illinois, southwesterly 500-hPa winds increased to around 25 ms^{-1} over an area with southeasterly surface winds and 500-1500 Jkg^{-1} of surface-based convective available potential energy (CAPE) creating a favorable environment for severe weather. In the favorable region, multiple tornadoes occurred, including one rated EF3 that caused considerable damage.

In the analysis, emphasis is placed on the role of the MCV in leading to a favorable environment for severe weather. In addition, convection-allowing forecasts of the MCV and associated environmental conditions from the 10-member Storm-Scale Ensemble Forecast (SSEF) system produced for the 2007 NOAA/Hazardous Weather Testbed Spring Experiment are compared to those from a similarly configured, but coarser 30-member convection-parameterizing ensemble. It was found that forecasts of the MCV track and associated environmental conditions (e.g., mid-level winds, low-level wind shear, and instability) were much better in the convection-allowing ensemble. Errors in the MCV track from convection-parameterizing members likely resulted from westward displacement errors in the incipient MCS. Furthermore, poor depiction of MCV structure and maintenance in convection-parameterizing members, which was diagnosed through a vorticity budget analysis, likely led to the relatively poor forecasts of the associated environmental conditions. The results appear to be very encouraging for convection-allowing ensembles, especially when environmental conditions lead to a high degree of predictability for MCSs which appeared to be the case for this particular event.

1. Introduction

Early theoretical predictability studies (e.g., Robinson 1967; Lorenz 1969; Smagorinsky 1969) indicated faster error growth with decreasing resolved scale, suggesting that forecast lead times for highly skillful deterministic forecasts at convective scales should be severely limited. These results are consistent with more recent studies documenting rapid error growth at convective scales in convection-allowing models (e.g., Kong et al. 2006, 2007; Zhang et al. 2006; Hohenegger and Schär 2007), and relatively poor warm season quantitative precipitation forecasting (QPF) over much of the United States (e.g., Fritsch and Carbone 2004) when the majority of rainfall is contributed by convective systems (e.g., Fritsch et al. 1986; Schumacher and Johnson 2006). For a more thorough review of predictability at convective scales see Lilly (1990) and Wandishin et al. (2008).

In contrast to the aforementioned studies, some work (e.g., Lilly 1990) has suggested that predictability limits for convective phenomena may be longer than those indicated by the early theoretical studies, especially over regions where convection tends to grow upscale into large organized mesoscale convective systems (MCSs) with circulations at scales much larger than the convective cells from which the systems originated. For example, Carbone et al. (2002) found that “episodes”, or time-space clusters of convective precipitation, with lifetimes up to 60 h were very common during the warm season over much of the US which resulted in coherent axes of radar echo frequencies when diurnally averaged time-longitude composites were constructed. Because the lifetime of these episodes is much longer than the individual convective systems, Carbone et al. (2002) suggest an “intrinsic predictability” associated with warm season rainfall that offers an opportunity for improved prediction

provided the propagation mechanisms of the episodes can be properly simulated by numerical weather prediction (NWP) models. Xue et al. (2001) demonstrated that a mesoscale model with 6 km grid-spacing was able to accurately predict with 48 h lead time a long squall line that formed out of much less organized convective cells and suggested predictability up to a two-day range for MCSs. In contrast, Davis et al. (2003) found that coarser-resolution operational NWP models could not reproduce the coherent rainfall axes present over the central US, attributing fundamental propagation errors to the use of cumulus parameterization (CP). Earlier work by Molinari and Dudek (1992) highlighted the difficulty in using CP to simulate organized convective systems by recognizing that, "*resolvable mesoscale structure develops from initially unresolvable cumulonimbus clouds*", and Bukovsky et al. (2006) suggest, because CPs act independently in individual model columns, realistic upscale growth of convective effects cannot occur.

Further hindering the ability of simulations using CP to accurately simulate the warm season rainfall climatology is the frequent occurrence of MCS-spawned mesoscale convective vortices (MCVs) over the central US which can influence the behavior of organized convection for multi-day periods (e.g., Johnston 1981; Bosart and Sanders 1981; Bartels and Maddox 1991; Fritsch et al. 1994; Trier et al. 2000a; Davis et al. 2002; Galarneau et al. 2009). MCVs are warm core mid- to lower tropospheric cyclonic circulations that usually develop within the stratiform region of MCSs (e.g., Zhang and Fritsch 1987; Menard and Fritsch 1989; Bartels and Maddox 1991; Bartels et al. 1997; Johnson and Mapes 2001; Skamarock et al. 1994; Davis and Galarneau 2009, hereafter DG09) and owe their existence to diabatic heating processes that result in mesoscale convergence of vorticity. The quasi-balanced nature of MCVs (e.g., Raymond and Jiang 1990; Davis and Weisman 1994; Trier and Davis 2002) has important implications for predictability because balanced flows are more predictable than unbalanced flows and constrain initial conditions for numerical models provided strong statistical relationships exist between the balanced fields (Davis and Trier 2007). Given that models using CP cannot reproduce the mesoscale circulations within well-organized MCSs that lead to MCV formation, simulations utilizing CP face difficulties in simulating MCV-related convective rainfall episodes.

In the current study, a case study approach will be used to compare convection-allowing to convection-parameterizing ensemble forecasts for a regional severe weather outbreak that was related to an MCV. Particular emphasis is placed on the role of the MCV in creating a favorable environment for severe weather, and how well convection-allowing and convection-parameterizing simulations were able to simulate the MCV. This case should represent a particularly challenging scenario for a forecast model because an accurate forecast is strongly dependent on the realistic simulation of preceding convection and its larger scale feedbacks. Because convection-allowing simulations better depict convective processes (e.g., Weisman et al. 2008), this is the type of case in which convection-allowing guidance could be most beneficial relative to guidance using CP. In addition, although many previous works have used numerical modeling to study various aspects of MCV formation and maintenance mechanisms (e.g., Rogers and Fritsch 2001; Davis and Trier 2002; Conzemius et al. 2007; DG09), only a few have examined the skill of numerical models in predicting MCVs in an operationally relevant context (e.g., Davis et al. 2002; Hawblitzel et al. 2007; Xue et al. 2009).

The paper is organized as follows: in section 2, data and methodology are provided, including model specifications; in section 3, a synopsis is given of the atmospheric conditions leading to the regional severe weather outbreak; in section 4, forecasts of various severe-weather-related fields are examined and compared to observations for members in both ensembles; in section 5, the vertical structure and maintenance of the observed and simulated MCV are explored through a vorticity budget analysis, and in section 6 summary and conclusions are provided.

2. Data and methodology

For much of the case study synopsis and vorticity budget analyses, operational 20-km grid-spacing Rapid Update Cycle (RUC) model analyses provided by NCEP and available at 1-hourly temporal resolution are used as "truth". The RUC analyses are generated using hourly intermittent 3DVAR assimilation cycles in which recent observations from various sources (e.g., wind profiler, radar, aircraft, surface METARS, satellite, etc.) are assimilated using the previous 1-hr RUC model forecasts as the background field (Benjamin et al. 2004a,b). Previous works (e.g., Davis et al. 2002; James and Johnson 2010) have documented the ability of RUC analyses in depicting MCVs. In addition, comparing RUC-derived to observed soundings, Thompson et al. (2003) found that the RUC analyses appeared accurate enough to serve as reasonable proxies for observed soundings in supercell environments. Thus, we feel that the RUC analyses are adequate for verifying general MCV features such as location, vertical structure, and intensity. However, the RUC analyses likely have problems depicting some vorticity generation processes in MCVs (discussed in Section 5), which is not surprising because MCVs are produced through convective-scale processes not well resolved by the 20-km RUC grid.

Convection-allowing simulations are examined from the 10-member, 4-km grid-spacing Storm-Scale Ensemble Forecast (SSEF) system which was run by the Center for Analysis and Prediction of Storms (CAPS) of the University of Oklahoma, and used by the 2007 NOAA/Hazardous Weather Testbed Spring Experiment (Xue et al. 2007; Kong et al. 2007). Convection-parameterizing forecasts are taken from a 30-member, 20-km grid-spacing ensemble run in post real-time at Iowa State University. Both ensembles consist of members using the WRF-ARW (version 2.2.0) model (Skamarock et al. 2005) that were initialized at 2100 UTC and integrated 33 hours over an approximately 3000 x 2500 km domain covering about two thirds of the continental United States (Fig. 1). For this particular case study, forecasts initialized at 2100 UTC May 31 2007 are examined. The 4-km SSEF system consists of five members with perturbed initial and lateral boundary conditions (ICs/LBCs) and mixed physics (ENS4; four perturbed members and one control member), while five other members use only mixed physics ($ENS4^{phys}$) so that impacts of the different physical parameterization schemes could be isolated (e.g., Schwartz et al. 2009). ENS4 and $ENS4^{phys}$ ensemble member specifications are provided in Tables 1 and 2, respectively. The 20-km ensemble is configured similar to the SSEF system, with 15-members having perturbed ICs/LBCs and mixed physics (ENS20), while 15 other members have only mixed physics ($ENS20^{phys}$). Note that ENS20 and $ENS20^{phys}$ have one more set of varied physics schemes relative to ENS4 and $ENS4^{phys}$, because in addition to the varied physics schemes included in the convection-allowing ensembles, the convection-parameterizing ensembles use three different CPs. However, 5-member subsets of ENS20 and $ENS20^{phys}$ using the same CP do have the same number of varied physics schemes as ENS4 and $ENS4^{phys}$. These 5-member subsets will be referred to as $ENS20_{cp}$ and $ENS20^{phys}{}_{cp}$ where CP refers to one of the three different cumulus parameterizations used: 1) Kain-Fritsch (KF; Kain and Fritsch 1993), 2) Betts-Miller-Janjic (BMJ; Betts 1986; Betts and Miller 1986; Janjic 1994), and 3) Grell-Devenyi (GD; Grell and Devenyi 2002). ENS20 and $ENS20^{phys}$ ensemble member specifications are provided in Tables 3 and 4, respectively.

For the SSEF control member, the 2100 UTC analyses from NCEP's operational North American Mesoscale (NAM; Janjic 2003) model (at 12-km grid-spacing) were used for ICs and the 1800 UTC NAM 12-km forecasts were used for LBCs. For the members with perturbed ICs, perturbations were extracted from ICs of the members from the 2100 UTC NCEP Short-Range Ensemble Forecast (SREF) system (Du et al. 2004) and added to the 2100 UTC NAM analyses. Corresponding SREF forecasts at three hour intervals were used for LBCs. Xue et al. (2007) and Kong et al. (2007) provide more details on the configurations. Different sets of ICs and corresponding LBCs for ENS20 and $ENS20^{phys}$ members were obtained directly from NCEP SREF members initialized at 2100 UTC. Both the convection-allowing and parameterizing ensembles used the RRTM short-wave

radiation scheme (Mlawer et al. 1997) and Goddard long-wave radiation scheme (Chou and Suarez 1994), along with the Noah land surface model (Ek et al. 2003). Varied PBL schemes include Mellor-Yamada-Janjic (MYJ; Mellor and Yamada 1982; Janjic 2002) and YonSei University (YSU; Noh et al. 2003) schemes. Varied microphysics schemes include Thompson et al. (2004), WRF single-moment 6-class (WSM-6; Hong and Lim 2006), and Ferrier et al. (2002), and surface layer schemes include Monin-Obukhov (Monin and Obukhov 1954; Paulson 1970; Dyer and Hicks 1970; Webb 1970) and Janjic Eta (Janjic 1996, 2002).

3. Synopsis of 1 June 2007 regional severe weather outbreak

The synoptic precursor for the 01 June 2007 regional severe weather outbreak was a broad mid-level trough that came onshore over the Pacific Northwest of the US on 28 May 2007. This trough moved slowly east, amplified, and eventually became cut off from the main branch of mid to upper level westerlies that transversed the periphery of a broad upper-level ridge in central Canada (Figs. 2a-e). This weather system and its associated surface features were responsible for multiple rounds of organized convection that initiated in the central High Plains (i.e., eastern Colorado; western Kansas and Nebraska) and propagated east preceding the 01 June event. The round of convection that was the impetus for the 01 June event initiated during the evening of 31 May. During the early morning of May 31, the cut-off upper low was virtually stationary over the western Dakotas (Fig. 2d). An associated surface low previously in western Minnesota retrograded to the west and became co-located with the upper low by 2100 UTC May 31, creating a vertically stacked system up to 200-hPa (not shown). During the same time period, southerly low-level winds began to advect air with higher equivalent potential temperatures (θ_e) northward into the high plains. The positive θ_e advection, combined with strong insolation, resulted in increasing instability beneath an axis of strong westerly mid-level winds (> 30 ms^{-1}) stretching from eastern Colorado through Kansas and northwest Missouri. This combination of environmental factors resulted in a favorable environment for strong organized convection centered over western Kansas, an area that was highlighted as having a moderate risk for severe weather in the Storms Prediction Center (SPC) Day 1 convective outlook (not shown).

Around 2100 UTC May 31, scattered convection developed across parts of Nebraska and Kansas. This convection moved east, slowly organizing and increasing in areal coverage. By 0600 UTC June 01, aided by a strengthening low-level jet over eastern Oklahoma and Kansas, the convection had congealed into a large leading line/trailing stratiform MCS with the leading edge of convective cells stretching from northeast Kansas in an arc toward south central Kansas and south into north central Oklahoma (Fig. 3). At about 0900 UTC, animations of composite reflectivity data from the WSR-88D radar network (see image archive at http://www.mmm.ucar.edu/imagearchive) revealed an area of cyclonic rotation behind the main convective line of the MCS and within the stratiform region in southeast Kansas. The cyclonic rotation in radar data reflected an MCV that moved northeast and was located over south central Iowa by 1500 UTC. Because the MCV was embedded within the outer periphery of the large 500-hPa cut-off low, a significant synoptic scale vorticity source, the disturbance is most appropriately termed a "hybrid" MCV case because ambient relative vorticity may have played a significant role in MCV genesis (Schumacher and Johnson 2009 also document hybrid MCVs). The hybrid cases are different from more traditional MCV cases documented in the literature which do not occur in association with a synoptic scale weather system and thus obtain cyclonic rotation from stretching of planetary vorticity. In fact, most MCVs occur within a mid-tropospheric ridge (Bartels and Maddox 1991; Trier et al. 2000a). Note, hereafter the disturbance will simply be referred to as an MCV.

During the time the MCV moved toward south central Iowa, most of the MCS dissipated over Missouri, northeast Arkansas, and western Oklahoma; however, convection was sustained around the

MCV and in a line arcing to the southeast of the MCV. The track of this MCV is easily inferred by the plot of maximum 600-hPa potential vorticity (PV) for the 09-21 UTC 01 June period in Fig. 2f, while the evolution of the incipient MCS and track of the MCV as inferred by the area of rotation in composite radar reflectivity data[1] is shown in Fig. 3. The vertical structure of the MCV during various stages of its life cycle is illustrated by vertical cross sections of PV and potential temperature (θ) in Fig. 4. At 0900 UTC, near the time when an area of rotation first became apparent in radar data, the PV anomaly as depicted by the RUC analyses was relatively shallow and confined to a ~200-hPa deep layer centered around 700-hPa at about 95 degrees W longitude (Fig. 4a). The vertically stacked cut-off upper low is reflected by the area of PV that extends to about 400-hPa centered near 104 degrees W longitude. By 1500 UTC, the PV anomaly had strengthened and covered a much deeper layer up to near the 400-hPa level with maximum PV values located near the 600-mb level (Fig. 4b). At 1800 UTC, the PV anomaly reached its peak intensity (Fig. 4c and e) and by 2100 UTC (Fig. 4d) the PV anomaly began to weaken. To illustrate temporal trends in the vertical structure of the PV anomaly, a time-height cross section using average θ and PV over a 3 degree longitude section centered over the area of maximum PV (from cross sections marked in Fig. 4f) is shown in Fig. 4e. From the time-height section it is clear the PV anomaly was most intense around 1800 UTC between the 600- and 500-hPa levels. As the MCV continued to track northeast through central Iowa after 1500 UTC, the environment downstream and along the southeast arcing convective line became increasingly unstable with increasing insolation. In addition, east-southeasterly winds at the surface veered to south-southwesterly just above the surface resulting in relatively large low-level shear vectors, and mid-level winds ahead of the 600-hPa short wave trough associated with the MCV had increased to almost 30 ms^{-1} (Figs. 5a-b).

At 1600 UTC, the cells located farthest southeast along the convective line extending from the MCV began to intensify into supercells, and during the period 1706-1726 UTC a tornado tracked through the towns of Grandview, Fruitland, and Muscatine in southeast Iowa. According to the post-storm damage assessment survey conducted by the Davenport, IA National Weather Service (NWS) Weather Forecast Office (WFO), damage in Grandview was rated EF3 and in Fruitland and Muscatine EF2. As the convective line continued to track northeast, other embedded supercells formed producing more tornadoes in eastern Iowa and northwest Illinois along with numerous severe wind gusts.

In addition to the aforementioned problems models using CP have simulating convective feedback to larger scales, DG09 note that it is difficult for models relying on CP to properly represent tilting of horizontal vorticity because such models often fail to produce sufficient negative buoyancy (Weisman and Davis 1998). Indeed, forecasts for this event from NCEP's operational North American Mesoscale (NAM) model (Janjic 2003) valid at 1800 UTC 01 June (Figs. 5c-d) did not suggest the very favorable conditions for severe weather over southeast Iowa and Illinois that were observed (Figs. 5a-b). In particular, the NAM forecasts did not forecast the well defined 600-hPa short-wave trough and associated enhanced mid-level flow over Iowa, Illinois, and Missouri, and the co-location of instability and wind shear just ahead of this short-wave trough over southeast Iowa. However, given the success of recent deterministic (e.g., Done et al. 2004; Weisman et al. 2008; Xue et al. 2009) and ensemble (e.g., Clark et al. 2009; Schwartz et al. 2009; Kong et al. 2009) convection-allowing WRF model simulations in forecasting organized convection, it is hypothesized that a convection-allowing ensemble could provide much improved forecasts of the environmental conditions associated with this event relative to a convection-parameterizing ensemble. Thus, convection-allowing and convection-parameterizing ensemble forecasts (model specifications listed in Tables 1 and 2) for this event are examined in the following section.

4. Comparison of convection-allowing and convection-parameterizing forecasts

[1] The composite radar reflectivity is from the WSI Corporation NOWrad product.

To examine forecasts of the mid-level flow, 21 h forecasts valid at 1800 UTC 01 June 2007 (within 1 h of when the first tornado occurred) of geopotential height, wind, and relative vorticity fields for the 600-hPa level are displayed for the ENS4 (Figs. 6a-e) and ENS20 (Figs. 6f-t) ensemble members (recall, these are the ensemble subsets with perturbed ICs and mixed physics). For comparison of these fields to the verifying RUC analyses, see Fig. 5b. In addition, probabilistic forecasts of 600-hPa wind speed greater than 20 ms^{-1}, ensemble mean 600-hPa geopotential height, and regions where wind speeds greater than 20 ms^{-1} were observed in the RUC analyses are illustrated in Figs. 6u-y for various ensemble subsets. Forecast probabilities are computed by finding the location of the verification threshold (20 ms^{-1}) within the distribution of ensemble member forecasts (Hamill and Colucci 1997, 1998). The area under the relative operating characteristic curve (ROC score; Mason 1982) was computed for the probabilistic forecasts (shown at bottom-right of Figs. 6u-y; for more details on how ROC score was computed see Clark et al. 2009). The ROC score is closely related to the economic value of a forecast system (e.g., Mylne 1999; Richardson 2000, 2001). ROC scores range from 0 to 1 with scores above 0.5 showing skill. Based on subjective examination of probabilistic precipitation forecasts, Buizza et al. (1999) suggest that 0.7 is the lower limit for a useful forecast.

The ENS4 members (Figs. 6a-e) all suggest some type of 600-hPa short wave trough centered over slightly different locations with an area of wind speeds greater than 20 ms^{-1} downstream from a vorticity maximum. The characteristics of the short-wave trough vary among the ENS4 members, but the location of the vorticity maximum and region of downstream enhanced wind speeds appear to cluster near the location at which these features were observed as shown in Fig. 5b. Furthermore, the correspondence of the ENS4 600-hPa wind speeds greater than 20 ms^{-1} to observations is reflected by probabilistic wind speed forecasts indicating that higher forecast probabilities match remarkably well to observations (Fig. 6u), which is also indicated by the 0.94 ROC score.

The forecast 600-hPa fields in the ENS20 members (Figs. 6f-t) appear to have much more variability than the ENS4 members (Figs. 6a-e), especially with respect to the location and amplitude of the short-wave trough. This higher variability is implied by the lower and more spread out forecast probabilities in ENS20 (Fig. 6v) relative to ENS4 (Fig. 6u). Furthermore, it is clear that the $ENS20_{BMJ}$ members (Figs. 6f-j) tend to forecast a noticeably weaker short-wave trough than the $ENS20_{KF}$ and $ENS20_{GD}$ ensemble members (Figs. 6k-t). The higher forecast probabilities from ENS20 and ENS20 subsets were displaced west of the region where 20 ms^{-1} wind speeds were observed (Figs. 6v-y), implying a westward displacement error in the forecasts of the 600-hPa short wave trough by most of the ENS20 members. Subjectively, it is clear that the ENS4 forecast probabilities provide better guidance than ENS20, and this better guidance is also suggested by the ROC scores that are markedly higher in ENS4.

A comparison of the forecasts from $ENS4^{phys}$ and $ENS20^{phys}$ (recall, these are the ensemble subsets with only mixed physics) for 600-hPa fields (Fig. 7) yields results similar to those from ENS4 and ENS20 (Fig. 6). Specifically, there is a clear tendency for the $ENS20^{phys}$ ensemble subsets to forecast the enhanced wind speeds ahead of the 600-hPa short-wave trough further west than what was observed which is clear from the probabilistic forecasts in Figs. 7v-y. Also, the $ENS20^{phys}_{BMJ}$ members (Figs. 7f-j) forecast a much weaker short-wave trough than $ENS20^{phys}_{KF}$ (Figs. 7k-o) and $ENS20^{phys}_{GD}$ members (Figs. 7p-t). However, there is much less variability or spread in the $ENS4^{phys}$ and $ENS20^{phys}$ forecasts relative to ENS4 and ENS20 which is expected since the former ensembles do not include IC perturbations. However, note that the $ENS4^{phys}$ probabilities of wind speeds greater than 20 ms^{-1} (Fig. 7u) still correspond well to observations.

To examine forecasts of low-level wind shear and instability, 21 h forecasts of the 10-m to 700-hPa shear vector magnitude (WSHR) and most unstable convective available potential energy

(MUCAPE) are displayed for the ENS4 (Figs. 8a-e) and ENS20 (Figs. 8f-t) ensemble members. For a comparison of these fields to the verifying RUC analysis, see Fig. 5a. In addition, probabilistic forecasts of WSHR greater than 16 ms^{-1} (P[WSHR>16]) and MUCAPE greater than 1000 Jkg^{-1} (P[MUCAPE>1000]) for various ensemble subsets are displayed in Figs. 8u-y and 8z-δ, respectively. Note that slightly different methods used to compute MUCAPE by the post-processors for ENS4 and ENS20 members and RUC analyses mean that the MUCAPE comparisons are not totally "clean"[2]. Thus, emphasis is placed on the spatial pattern in the MUCAPE fields, rather than the magnitude of values which should exhibit the largest impact from the use of the different methods.

Subjectively, the low-level wind pattern and spatial distribution of MUCAPE and WSHR appear to resemble the RUC analysis (Fig. 5a) most closely in the cn (Fig. 8a) and p1 (Fig. 8b) ENS4 members. In these members, higher values of MUCAPE extend from southern and eastern Missouri and arc into southeast Iowa where the higher MUCAPE values are co-located with a maximum in WSHR. Also, in both the cn and p1 members, there is a relatively strong MUCAPE gradient in southern Iowa/northern Missouri which also resembles the RUC analysis. The distribution of MUCAPE and WSHR is consistent with the conceptual MCV model developed by Raymond and Jiang (1990), which was demonstrated quantitatively by Trier et al. (2000b), in which mid-level isentropic ascent (descent) having a destabilizing (stabilizing) effect is favored downshear (upshear) of the mid-level vortex. Some of the other ENS4 members have less resemblance to the RUC analyses, despite having a similar placement of the mid-level short-wave trough. Differences in the vertical structure of the simulated disturbance (examined later), which are not apparent from the 600-hPa level, likely result in the different MUCAPE/WSHR spatial patterns for these members (Figs. 8c-e).

The spatial distribution of the MUCAPE and WSHR fields for the ENS20 members (Figs. 8f-t) appears to resemble the RUC analyses much less than the ENS4 members. The $ENS20_{BMJ}$ members (Figs. 8f-j) underforecast WSHR and their MUCAPE fields do not have a relative minimum in eastern Kansas/western Missouri as in the RUC analysis. Opposite the behavior of the $ENS20_{BMJ}$ members, many of the $ENS20_{KF}$ and $ENS20_{GD}$ members tend to overforecast WSHR. In addition, in the $ENS20_{BMJ}$ and $ENS20_{GD}$ members, the highest values of MUCAPE were forecast to the south and west of the WSHR maxima, unlike the RUC analyses in which a local minimum in MUCAPE was observed south and west of the highest values of WSHR. However, member 09 (Fig. 8n) appears to be a notable exception to the aforementioned MUCAPE/WSHR errors, and the member 09 600-hPa geopotential heights and wind speeds (Fig. 6n) also correspond much better with the RUC analysis than the other ENS20 members.

The P[WSHR>16] forecasts (Figs. 8u-y) generally reflect the tendencies in the members composing each ensemble subset. In ENS4, the highest P[WSHR>16] generally coincide with observations (Fig. 8u), while clear westward biases are evident in ENS20 and ENS20 subsets. Furthermore, the ROC score for the ENS4 P[WSHR>16] of 0.88 is noticeably higher than all of the ENS20 ensemble subsets, whose ROC scores range from 0.42 to 0.80.

The P[MUCAPE>1000] forecasts (Figs. 8z-δ) are a bit more difficult to evaluate subjectively since many of the ENS4 and ENS20 members overforecast MUCAPE>1000 resulting in large areas of non-zero P[MUCAPE>1000] over much of the domain. However, the highest P[MUCAPE>1000] values in ENS4 generally are co-located with the highest observed values roughly centered over Illinois. In contrast, the highest values in ENS20 are displaced further to the west in eastern Kansas

[2] In RUC, MUCAPE is computed using the most buoyant parcel within 300 hPa of the surface without using a virtual temperature correction (e.g., Doswell and Rasmussen 1994). Before the most buoyant level is determined, an averaging of potential temperature and water vapor mixing ratio is applied to the lowest seven native RUC levels (~45 – 55 hPa). In the ENS4 members, a water loading correction and virtual temperature correction are applied and the parcel with the highest θ_e on the native vertical coordinate within the bottom 300 hPa is used to compute MUCAPE. For the ENS20 members, the virtual temperature correction is applied, parcels are defined as 500-m layer average quantities, and the parcel with the highest θ_e within the bottom 3 km is used to compute MUCAPE.

and western Missouri. This subjective impression is consistent with the ENS4 ROC score of 0.80 for P[MUCAPE>1000], which is noticeably higher than ROC scores for the ENS20 ensemble subsets which range from 0.58 to 0.71.

A comparison of WSHR and MUCAPE forecasts from ENS4^{phys} and ENS20^{phys} in Fig. 9 shows similar trends as those discussed for Fig. 8. However, as was noted for the 600-mb fields, it is clear that there is much less spread in the ENS4^{phys} and ENS20^{phys} forecasts since they do not have IC or LBC perturbations. Interestingly, all of the ENS4^{phys} members appear to have a spatial distribution of MUCAPE and WSHR fields in which a maximum in SRH is located in southwest Iowa co-located with the northern/western end of relatively high MUCAPE values, a spatial pattern very similar to what is seen in the RUC analysis (Fig. 5a). However, all of the ENS4^{phys} members had a small southwest displacement error for the northern end of the higher WSHR values which is clearly seen by P[WSHR>16] in Fig. 9u.

Summarizing the results for the comparison of the convection-allowing and convection-parameterizing forecasts, it is clear that the convection-allowing forecasts had an advantage relative to the convection-parameterizing forecasts. Furthermore, the superior convection-allowing forecasts were clearly related to a better forecast of an MCV and its impact on the larger scale flow. It is also worth noting that the simulated reflectivity fields in most of the convection-allowing forecasts correctly depicted the observed convective mode (not shown). In the following section, the vertical structure and maintenance of the mid-level perturbation in the ensemble members will be explored in an attempt to diagnose deficiencies in the forecasts.

5. Vorticity budget analyses

A vorticity budget for the MCV as depicted in the 1-hourly RUC analyses and in the ensemble member simulations was computed using the flux form of the vorticity equation as described by DG09:

$$\frac{\partial \zeta}{\partial t} = -\nabla \cdot \left(\boldsymbol{V}\eta - \omega \widehat{\boldsymbol{k}} \times \frac{\partial \boldsymbol{V}}{\partial p} - \widehat{\boldsymbol{k}} \times \boldsymbol{F} \right) \quad (1)$$

where ζ is the relative vorticity, $\boldsymbol{V}$ the horizontal wind vector, η the absolute vorticity, ω the vertical velocity in pressure coordinates, and $\boldsymbol{F}$ the frictional force. It can be easily shown that familiar terms from the traditional form of the vorticity budget equation fall out when the divergence operator in (1) is applied to the first term in brackets yielding stretching and horizontal advection of vorticity and to the second term yielding vertical advection and tilting. Also, note that the divergence is only in the horizontal plane. Integrating (1) over a closed region, applying Gauss's theorem (or the divergence theorem), and neglecting friction[3] yields:

$$\frac{\partial C}{\partial t} = -\oint \eta \boldsymbol{V} \cdot \widehat{\boldsymbol{n}} dl + \oint \omega \left(\widehat{\boldsymbol{k}} \times \frac{\partial \boldsymbol{V}}{\partial p} \right) \cdot \widehat{\boldsymbol{n}} dl$$

$$\frac{\partial C}{\partial t} = -\oint \eta \boldsymbol{V} \cdot \widehat{\boldsymbol{n}} dl + \oint \omega \left(\widehat{\boldsymbol{k}} \times \frac{\partial \boldsymbol{V}}{\partial p} \right) \cdot \widehat{\boldsymbol{n}} dl \quad (2) \quad 2)$$

where C is the circulation about the boundary of the closed region. For both terms on the right hand side (RHS) of (2), only the component normal to the boundary of the closed region is considered when evaluating the circulation tendency within the region. Thus, as noted by DG09, the form of (2) is very useful because circulation tendency within a region can be evaluated without explicitly considering

[3] Because the budget analyses are restricted to 900-hPa and above which is well removed from the surface at most times, the effect of friction is likely negligible. Furthermore, the neglect of friction does not appear to be detrimental to the proceeding budget analyses consistent with similar budgets computed by DG09.

complex and fine scale vorticity dynamics within the region. Furthermore, decomposing the first RHS term of (2) into mean and eddy contributions by using the divergence theorem to relate the average wind component normal to the boundary of the region to the mean divergence over the area of the region yields:

$$\frac{\partial C}{\partial t} = -\bar{\eta}\tilde{\delta}A - \oint \eta' \boldsymbol{V}' \cdot \hat{\boldsymbol{n}} dl + \oint \omega \left(\hat{\boldsymbol{k}} \times \frac{\partial \boldsymbol{V}}{\partial p} \right) \cdot \hat{\boldsymbol{n}} dl \quad (3)$$

where A is the area of the region, $\tilde{\delta}$ the mean divergence over A, $\bar{\eta}$ the average vorticity around the perimeter of the region, and η' and $\boldsymbol{V}'$ are perturbations relative to mean values around the perimeter of the region. The mean term [first RHS term of (3)] represents vortex stretching while the eddy flux [second RHS term of (3)] represents horizontal vorticity advection. DG09 provide a physical interpretation of the third RHS term of (3) which is often referred to as simply tilting, but actually represents a combination of tilting and vertical vorticity advection. Basically, this term can be thought of as tilting of the component of horizontal vorticity normal to the boundary of the region by vertical motion along the boundary. For a horizontal vortex line directed into the region, an updraft along the boundary of the region would lift the vortex line decreasing (increasing) vertical vorticity inside (outside) the region. Hereafter, the third RHS term is simply referred to as tilting. The three RHS terms of (3) are computed for the budget analyses, and all terms are divided by the area of the region to obtain vorticity, rather than circulation tendency. In addition, to evaluate the "balance" of the vorticity budget, the LHS was computed as $\partial\varsigma / \partial t = (\varsigma_{t+\Delta t} - \varsigma_t) / \Delta t$ and compared to the average of the RHS terms at t and $t+\Delta t$ where Δt is chosen as 3600 s.

For forecast hours 4 to 32, which encompassed the life cycle of the observed MCV, the budget was computed in observations and simulations for a 340-km x 340-km grid centered on the MCV at vertical levels every 25-hPa from 900- to 400-hPa. The center point of the grid box was manually chosen to try to maximize the average relative vorticity within the box. For the first few forecast hours before the MCV was discernible, the grid was centered over the area of convection from which the MCV appeared to emanate. The 340-km distance was chosen because it appeared to be the minimum distance required to encompass most of the MCV-related vorticity maxima in RUC analyses and model simulations. The MCVs were tracked manually by displaying plots of the average relative vorticity in the 400- to 700-hPa layer. To avoid tracking any vorticity maxima unrelated to convection, the relative vorticity plots were overlaid by 1-hourly accumulated precipitation and only vorticity maxima that obviously emanated from an area of convection as inferred by the precipitation fields were tracked. For tracking in both models and analyses, the horizontal wind fields were filtered to remove wavelengths below 160-km before computing vorticity, allowing easier identification of coherent MCV-related vorticity regions, which was especially useful for the 4-km grid-spacing simulations that contained very noisy raw vorticity fields. This filter was not used for the actual vorticity budget analysis.

The tracks of the manually identified MCVs are shown in Figure 10. The tracks are only shown for times at which an MCV or developing MCV was discernible from the 700- to 400-hPa layer averaged vorticity. Because these were all "cold-start" runs (i.e., model dynamics start off with an unsaturated initial state) and convection had only just begun to initiate at the time of initialization, simulated MCV tracks did not become identifiable until 4 to 10 hours into the forecasts. The 20-km ensemble members generally have tracks displaced to the west of the observed MCV track, while 4-km ensemble members have tracks generally clustered around the observed track. The MCV displacement errors in the 20-km members are likely related to westward displacement errors in the simulated MCV-producing convective systems (not shown), which is consistent with previous studies documenting the

inability of models using convection-parameterizing grid-spacing to property simulate MCS structure and propagation (e.g., Davis et al. 2003; Clark et al. 2009).

The ENS4 and ENS20 MCV tracks (Fig. 10a) have more spread than the $ENS4^{phys}$ and $ENS20^{phys}$ tracks (Fig. 10b), similar to parameters examined in the previous section. Average displacement errors for the MCV at forecast hour 18 (1500 UTC) are 72 km for ENS4, much less than in ENS20 and ENS20 subsets which range from 125 to 275 km (Fig. 10a), and 46 km for $ENS4^{phys}$, also less than in $ENS20^{phys}$ and $ENS20^{phys}$ subsets which range from 60 to 160 km.

At each forecast hour the MCV was discernible in analyses and simulations, the vorticity budget terms along with the actual relative vorticity at each vertical level were averaged over the 340 km x 340 km grid box to construct time-height diagrams. The time-height diagrams for each ensemble member and the analyses can be found at a supplemental website http://www.meteor.iastate.edu/~clar0614/vort_budget. The budget for the RUC analysis is displayed in Figure 11. Note that regions in time-height space that contained below ground pressure levels are simply assigned missing values, which is indicated by the white space at the bottom-left of the time-height plots. The balance of the budget in the RUC analyses as inferred from a comparison between time-height spatial distributions of vorticity tendency [LHS of Eq. (3); Fig. 11a] and the sum of tendency terms [RHS of Eq. (3); Fig. 11b] is fairly good, with a spatial correlation coefficient of 0.61. Relatively large differences between vorticity tendency and the sum of tendency terms likely occur when large relative adjustments are made to the background vorticity field based on recent observations. When these adjustments occur, the vorticity budget balance is "upset" because the vorticity field changes in response to something other than a physical process (i.e., vorticity changes do not result from one of the vorticity tendency terms) and it can be inferred that the RUC analysis contains errors in one or more tendency terms. Errors in the vorticity budget balance are also contributed by the relatively large Δt used to compute the time derivative. The largest differences between vorticity tendency and the sum of tendency terms occur near 10 or 11 UTC between 600 and 400-hPa. At this time, the vorticity tendency (Fig. 11a) was noticeably larger than the sum of tendency terms (Fig. 11b), implying that one or more tendency terms were underestimated in the RUC analyses. These errors should be kept in mind when subsequent comparisons are made between ensemble member simulations and the RUC analyses. Note that the balance of the vorticity budgets in the ensemble member simulations are much better than in the RUC analyses (correlation coefficients are shown in Figs. 15 and 16 which are discussed later) because the simulated vorticity tendencies result solely from modeled physical processes (i.e., observations are not assimilated).

By far, the largest contribution to positive vorticity tendency in the RUC analyses is from vortex stretching (Fig. 11c), consistent with MCV genesis mechanisms found in previous works (e.g., Zhang 1992; DG09). The stretching term is maximized between 600 and 400-hPa around 10 or 11 UTC, which matches the time at which the stratiform region in the observed MCS appeared to be the most extensive in the observed reflectivity fields (not shown). Beneath the area of maximum stretching, stretching is negative which likely reflects divergence from a low-level cold pool generated by the MCS. Only about four hours later (~ 1500 UTC), the sign of the stretching term in the mid-levels becomes negative as the observed MCS weakened and the entire area of stratiform precipitation rapidly dissipated (not shown). However, at the same time, stretching switches from negative to positive at low-levels so that the maximum vorticity begins to shift to lower levels (Fig. 11f). DG09 observed very similar time-height spatial distributions of stretching in two simulated cases they examined (see their Figs. 10d and i) and attributed the switch from divergence to convergence at low-levels to the impact that the MCS/MCV had on the net change in moist static energy with height, which resulted in a moist and near neutrally stable environment during the morning following MCV formation. In our case, an analogous change to moist and neutrally stable conditions likely allowed the small line of convection that was maintained immediately downstream of the MCV to become "surface

based" (i.e., the parcels composing the convective updrafts likely originated near the surface), and low-level convergence into the line of convection likely led to positive contributions to vorticity tendency from vortex stretching.

Vorticity tendency time-height diagrams are also shown for $ENS20_{bmj}$ member 02 (Fig. 12), $ENS20^{phys}$ member 27 (Fig. 13), and ENS4 member p1 (Fig. 14). These members are displayed because they contain features fairly representative of the other ensemble members in their respective subsets. In member 02, the time-height spatial pattern in the sum of the tendency terms (Fig. 12b) is, in some ways, similar to the RUC analysis (Fig. 11b). For example, during the first part of the forecast, positive vorticity tendencies in the mid-troposphere occur above negative tendencies at low-levels, and the pattern is reversed near 1500 UTC. Furthermore, also similar to the RUC analyses, the vorticity tendencies in member 02 are dominated by stretching (Fig. 12c); with the eddy flux (Fig. 12d) and tilting terms (Fig. 12e) also making noticeable contributions during the first part of the forecast. However, differences in the magnitude of tendency terms in member 02 result in time-height patterns in vorticity (Fig. 12f) drastically different from the RUC analyses (Fig. 11f). In particular, weaker stretching in member 02 relative to RUC analyses results in a mid-level vortex that is much weaker, and the prolonged period of negative stretching at low-levels leads to negative low-level vorticity below the mid-level vorticity maximum, whereas RUC analyses indicated that low-level vorticity remained positive below the mid-level vorticity maximum. It is notable that the only ENS20 or $ENS20^{phys}$ members that contained large negative low-level stretching tendencies were those that used BMJ. These negative tendencies are consistent with the unusual convective heating profiles produced by the BMJ that have been examined in detail by Bukovsky et al. (2006) and were found to lead to mesoscale downdrafts that diverge just above the surface rearward from areas of parameterized convection. Bukovsky et al. (2006) noted that propagating systems resulting from these mesoscale downdrafts are usually spurious, but that some aspects of the simulated propagation mechanisms may be similar to those of observed convective systems. Negative low-level tendencies during the first part of the member 02 forecast as well as the RUC analyses were also contributed by the eddy flux term (Fig. 12d). These results contrast with the cases simulated by DG09 in which the eddy flux at low-levels was strongly positive resulting from the transport of vorticity along the edge of an outflow boundary to beneath the mid-level vortex.

The vorticity tendency time-height diagrams for ensemble member 27 (Fig. 13) are very different than those for member 02 (Fig. 12) and from the RUC analyses (Fig. 11). For example, near the beginning of the forecast (~ 0600 UTC), the sum of tendency terms in member 27 (Fig. 13b) is positive over the entire depth of the 900- to 400-hPa layer, unlike member 02 and the RUC analyses where the positive tendencies are confined to above around 750-hPa. The most striking difference in member 27 is in the stretching term (Fig. 13c), which is strongest for most of the forecast period over only the lowest layers of the troposphere examined (generally between 900- and 750-hPa), and is in stark contrast to member 02 and the RUC analyses which contain maxima in stretching in the mid-troposphere from about 0300 to 1200 UTC and at low-levels for a period after 1200 UTC. During the initial spin-up of the MCV (~ 0600 UTC), tilting (Fig. 13e) actually contributes more to mid-level positive vorticity tendencies than stretching (Fig. 13c) for member 27. The sum of member 27 vorticity tendencies results in a maximum vorticity center much lower (~ 800-hPa) relative to the RUC analyses and relative to what is typically observed in MCVs. The behavior in the stretching term observed in member 27 is also typical of other members examined in this study that use the GD cumulus parameterization as well as members that use KF. Without having examined the simulations in more detail (which is beyond the scope of this study), we can only speculate that the unusual time-height spatial distribution in the stretching terms for these members is related to convective heating profiles generated by the cumulus parameterizations and a failure to produce divergent low-level cold pools.

For ensemble member p1 (Fig. 14), the time-height vorticity tendencies contain many features that match up well with the RUC analyses. For example, the total vorticity tendency [i.e., the sum of Eq. (3) RHS terms; Fig. 14b] is strongly positive in the mid-troposphere during the first part of the forecast with negative total tendencies occurring underneath; a pattern that reverses after about 1200 UTC similar to the RUC analyses. Also, the stretching term (Fig. 14c) makes the largest relative contributions to the total vorticity tendencies, with the tilting (Fig. 14e) and eddy flux terms (Fig. 14d) also making noticeable contributions, especially during the first part of the forecast. The pattern in the member p1 stretching term is very similar to that observed in the simulations analyzed by DG09 as well as the RUC analyses. Furthermore, the other ENS4 and ENS4^{phys} members exhibit similar time-height distributions in the stretching term (not shown) and generally appear to have the most realistic depictions of the individual forcing terms. To obtain a more general picture of which budget terms contributed most to total vorticity tendency, all three forcing terms were summed at points in time-height space where the total vorticity tendency was positive and negative, respectively (gray shaded and black outlined bars, respectively, in Figs. 15 and 16). Clearly, stretching is the dominant contributor to positive vorticity tendencies for all ensemble members as well as RUC analyses. In addition, the eddy flux term was the dominant contributor to negative tendencies in most members as well as RUC analyses; however, note that stretching also made a relatively large contribution to negative tendencies in the RUC analyses. In the subsequent analyses, additional summary statistics of budget terms are presented to gauge the overall behavior of the ensembles, which more clearly suggest the superior performance of ENS4 and ENS4^{phys} members in simulating the MCV structure and maintenance mechanisms.

To evaluate how well the ensemble members simulate the amplitude of the MCV, time series of the maximum vorticity over the 900- to 300-hPa layer from the time-height plots (e.g., Figs. 11-14) are displayed in Figures 17a-c. The ENS4 and ENS4^{phys} members (Fig. 17a) do a reasonable job of predicting the maximum vorticity, but most of the members under-predict the maximum vorticity during the time period when the MCV was most intense (~ forecast hours 15-18). The ENS20 and ENS20^{phys} members (Fig. 17b and c) using KF and GD cumulus parameterizations do about as well as the ENS4 and ENS4^{phys} members (Fig. 17a) at simulating the maximum vorticity, but the BMJ members severely under-predict the maximum vorticity, consistent with the vorticity fields previously discussed in Figs. 6f-j and Figs. 7f-j. Although KF and GD members appear capable of simulating the correct MCV amplitude, they simulate the maximum vorticity at lower levels than in RUC analyses (Figs. 17e and f), unlike the ENS4 and ENS4^{phys} members which correspond quite well to the RUC analyses (Fig. 17d). Furthermore, although *not* capable of simulating the correct MCV amplitude, the BMJ members actually do reasonably well at simulating the correct level of maximum vorticity. In summary, none of the ENS20 or ENS20^{phys} subsets can accurately simulate both the maximum vorticity and the level at which the maximum vorticity occurs, while the ENS4 and ENS4^{phys} do appear capable of simulating both of these MCV features. Based on the time-height diagrams (Figs. 12 and 13), the errors in the ENS20 and ENS20phys members appear to be most related to the stretching term. For KF and GD members, the stretching term is maximized in the lower troposphere resulting in an MCV that is too shallow, while the stretching term in the BMJ members is maximized in the mid-troposphere but is too weak resulting in a correspondingly weak MCV.

Times series of vorticity tendencies contributed by stretching averaged over three different layers (900-800-hPa, 800-600-hPa, and 600-400-hPa) for the ENS4^{phys} and ENS20^{phys} ensemble members and RUC analyses (Fig. 18) clearly show the superiority of the ENS4^{phys} members as well as the sensitivity of the ENS20^{phys} members to the different cumulus parameterizations. However, there are some noticeable differences between ENS4^{phys} members and RUC analyses; for example, peak tendencies in ENS4^{phys} for the 600-400-hPa layer (Fig. 18a) occur two or three hours earlier than in RUC, and the tendencies during forecast hours 15 to 19 for the 800- to 600-hPa layer do not become

negative in ENS4^{phys} as they do in RUC analyses. For the ENS20^{phys} member stretching tendencies, the KF and GD members all have the highest values in the lowest layer (Fig. 18f; 900 to 800-hPa), and while the BMJ members contain negative stretching tendencies in the 900-800-hPa layer, the minima occur 4-hrs earlier than in RUC analyses.

6. Summary and discussion

MCVs can influence the behavior of organized convection for multi-day periods. Thus, in order to accurately simulate convection associated with MCVs and their impacts on the large scale environment, NWP models must be able to properly simulate MCV dynamics and maintenance. Because models using cumulus parameterization (CP) have major difficulties in simulating mesoscale circulations within well organized MCSs that lead to MCV formation, it is expected that models using CP will struggle to simulate MCVs and associated weather.

In this study, an analysis of an MCV-related regional severe weather outbreak that occurred on 1 June 2007 in eastern Iowa and northwest Illinois was performed. It was shown that enhanced mid-level winds and low-level shear downstream from and along a southwest arcing line of convection associated with an MCV lead to favorable conditions for rotating updrafts after a combination of insolation and MCV-induced vertical motion led to modest destabilization. In these favorable severe weather conditions, multiple tornadoes were reported.

Subsequent analyses examined forecasts of this event from 4-km grid-spacing convection-allowing and 20-km grid-spacing convection-parameterizing ensembles. It was found that forecasts of mid-level winds, low-level severe parameters (MUCAPE and wind shear), and the MCV track were much better in the convection-allowing ensemble members. Relatively large westward displacement errors in the MCV track for convection-parameterizing forecasts were likely related to the inability of these members to properly simulate the propagation mechanisms of the MCV-spawning MCS, which resulted in simulated convective systems that moved too slowly eastward during and prior to generating the MCV. Furthermore, we speculate that the errors in the low-level severe parameters for the convection-parameterizing members, especially low-level wind shear, may have been related to the unrealistic vertical structures in the simulated MCVs. In particular, the low levels at which the MCV was centered in the CP runs (e.g., ~ 750-hPa) could have led to much greater low-level wind shear relative to simulations in which the MCV was centered higher in the mid-troposphere (e.g., ~ 600-hPa). Conceptually, this makes sense if one considers two idealized MCVs of similar intensity and near surface conditions. If one of the MCVs is centered lower in the troposphere, the low-level winds beneath this MCV must increase faster with height resulting in higher low-level wind shear. Through a vorticity budget analysis it was found that the unrealistic vertical structures in the convection-parameterizing members were mostly related to the stretching tendencies, which were generally too weak in BMJ members and too shallow and close to the ground throughout most of the KF and GD member simulations.

Although much of the emphasis in this study was placed on the impact of the different model physics on the forecasts of the MCV and severe weather environment, it should also be emphasized that IC/LBC perturbations clearly had a larger impact on the forecasts than mixed physics. In fact, in a related study (Clark et al. 2010) examining a larger set of cases with the same ensemble configurations, it was found that the mixed physics only ensembles contained a small portion (5 – 15%) of the ensemble spread that the mixed physics and perturbed IC/LBC ensembles contained for fields like geopotential height and mean-sea-level pressure. Nonetheless, despite the large relative impact of different ICs among the members from each ensemble, it is unlikely that the difference in ICs *between* ENS4 and ENS20 was the most important factor contributing to the difference in forecast quality. Recall, both ENS4 and ENS20 used similar IC perturbations from NCEP's SREF system. In ENS4,

these perturbations increase ensemble spread relative to ENS4^{phys}, but do not introduce any systematic errors. In contrast, the ENS20 forecasts with perturbed ICs/LBCs have the same systematic errors (e.g., westward displacement errors for the MCV) as the mixed physics only ENS20^{phys} configuration (along with the increase in ensemble spread). Thus, the errors in ENS20 clearly result from something other than the ICs. The evidence presented herein suggests that these errors are caused by the inability of the convection-parameterizing simulations to properly depict an MCV-producing MCS and its "imprint" on the larger scale environment.

Because this paper is a case study, we stress that it is difficult to assess the generality of the results. In addition, it is not known how frequently similar "hybrid" MCVs occur and we are not aware of any attempts in the literature to document their climatology relative to "traditional" MCVs. In addition, because of the relative predictability associated with most synoptic scale disturbances, hybrid MCVs might be more predictable than traditional MCVs that are not linked to a distinct synoptic scale weather system and typically occur with weak forcing. This idea is supported by an evaluation conducted by Xue et al. (2009) of convection-allowing ensemble forecasts from the 2009 NOAA/HWT Spring Experiment of a very intense derecho-producing MCV that developed 8 May 2009 immediately downstream of a mid-level short wave trough. The ensemble forecasts for the 8 May 2009 case were also found to be very skillful and suggested a large degree of forecast certainty for the MCV and incipient MCS. Clearly, these issues present many potential avenues for future work.

At the least, this case study serves as an example of the advantages afforded by convection-allowing forecasts. Typically, forecasts in environments containing ongoing convection from NWP models using CP are associated with a high degree of uncertainty because "convective feedbacks", (i.e., spurious tendencies resulting from activation of CPs) are thought to "contaminate" the forecasts (e.g., Baldwin et al. 2002; Correia et al. 2004). However, convection-allowing forecasts that more accurately simulate convective processes and impacts on the larger scale flow may be less likely to be negatively impacted by ongoing convection. Nonetheless, the inherent uncertainty and rapid error growth associated with convective-scale processes should still yield a high degree of uncertainty in cases when convection is present, although the convection-allowing forecasts examined herein appeared to have relatively low forecast uncertainty. It is hypothesized that certain large scale regimes are associated with greater MCS predictability, with the event examined herein an example of such a case. In fact, this case occurs in the middle of what Germann et al. (2006) refer to as a "Lagrangian persistence corridor", or region with apparently enhanced predictability for MCSs. In these types of cases/regions, convection-allowing simulations could be particularly advantageous relative to convection-parameterizing forecasts that are unable to properly simulate convective impacts on the larger scale flow.

Acknowledgments The authors would like to thank Huiling Yuan at the Global Systems Division of the Earth System Research Laboratory (ESRL GSD) for assistance in obtaining SREF data in post real-time. This particular research was funded by NSF Grants ATM-0537043 and ATM-0848200. Additional support was provided through a National Research Council Post-doctoral Award for the first author under the guidance of David Stensrud. The ENS20 simulations were conducted on the 64-processor computing cluster in the meteorology program at ISU. The CAPS real-time 4-km ensemble forecasts were primarily supported by the NOAA CSTAR program. Supplementary support was provided by NSF ITR project LEAD (ATM-0331594). Xue was also supported by NSF ATM-0530814 and ATM-0802888. Drs. Kelvin K. Droegemeier, Keith Brewster, John Kain, Steve Weiss, David Bright, Matt Wandishin, Mike Coniglio, Jun Du, Jimy Dudhia, Morris Weisman, Greg Thompson and Wei Wang contributed to the ensemble system design and WRF model configuration and Kevin Thomas carried out the CAPS real-time runs. The CAPS real-time predictions were performed at the Pittsburgh Supercomputing Center (PSC) supported by NSF. The WSI NOWrad data were obtained

from the Global Hydrology Resource Center at the Global Hydrology and Climate Center in Huntsville, Alabama.

References

Baldwin, M. E., J. S. Kain and M. P. Kay, 2002: Properties of the convection scheme in NCEP's Eta model that affect forecast sounding interpretation. *Wea. Forecasting*, **17**, 1063-1079.

Bartels, D. L., and R. A. Maddox, 1991: Midlevel cyclonic vortices generated by mesoscale convective systems. *Mon. Wea. Rev.*, **119**, 104–118.

——, J. M. Brown, and E. I. Tollerud, 1997: Structure of a midtropospheric vortex induced by a mesoscale convective system. *Mon. Wea. Rev.*, **125**, 193–211.

Benjamin, S. G., G. A. Grell, J. M. Brown, T. G. Smirnova, and R. Bleck, 2004: Mesoscale weather prediction with the RUC hybrid isentropic–terrain-following coordinate model. *Mon. Wea. Rev.*, **132**, 473–494.

——, D. Dévényi, S. S. Weygandt, K. J. Brundage, J. M. Brown, G. A. Grell, D. Kim, B. E. Schwartz, T.G. Smirnova, T.L. Smith, and G.S. Manikin, 2004: An hourly assimilation–forecast cycle: The RUC. *Mon. Wea. Rev.*, **132**, 495–518.

Betts, A. K., 1986: A new convective adjustment scheme. Part I: Observational and theoretical basis. *Quart. J. Roy. Meteor. Soc*., **112**, 677-691.

——, and M.J. Miller, 1986: A new convective adjustment scheme. Part II: Single column tests using GATE wave, BOMEX, ATEX and Arctic air-mass data sets. *Quart. J. Roy. Meteor. Soc.,* **112**, 693-709.

Bosart, L. F., and F. Sanders, 1981: The Johnstown flood of July 1977: A long-lived convective system. *J. Atmos. Sci.*, **38**, 1616–1642.

Buizza, R., A. Hollingsworth, F. Lalaurette, and A. Ghelli, 1999: Probabilistic predictions of precipitation using the ECMWF Ensemble Prediction System. *Wea. Forecasting*, **14**, 168–189.

Bukovsky, M. S., J. S. Kain, and M. E. Baldwin, 2006: Bowing convective systems in a popular operational model: Are they for real? *Wea. Forecasting*, **21**, 307-324.

Carbone, R. E., J. D. Tuttle, D. A. Ahijevych and S. B. Trier, 2002: Inferences of predictability associated with warm season precipitation episodes. *J. Atmos. Sci*., **59**, 2033–2056.

Chou M.-D., and M. J. Suarez, 1994: An efficient thermal infrared radiation parameterization for use in general circulation models. NASA Tech. Memo. 104606, 3, 85pp.

Clark, A. J., W. A. Gallus, and T. C. Chen, 2007: Comparison of the diurnal precipitation cycle in convection-resolving and non-convection-resolving mesoscale models. *Mon. Wea. Rev.*, **135**, 3456–3473.

——, W. A. Gallus, M. Xue, and F. Kong, 2009: A comparison of precipitation forecast skill between small convection-allowing and large convection-parameterizing ensembles. *Wea. Forecasting*, **24**, 1121–1140.

——, ——, ——, and ——, 2010: Growth of spread in convection-allowing and convection-parameterizing ensembles. *Wea. Forecasting* (In press).

Coniglio, M. C., K. L. Elmore, J. S. Kain, S. J. Weiss, M. Xue, and M. L. Weisman, 2009: Evaluation of WRF model output for severe-weather forecasting from the 2008 NOAA Hazardous Weather Testbed Spring Experiment. *Wea. Forecasting* (In Press).

Conzemius, R. J., R. W. Moore, M. T. Montgomery, and C. A. Davis, 2007: Mesoscale convective vortex formation in a weakly sheared moist neutral environment. *J. Atmos. Sci.*, **64**, 1443–1466.

Correia, J., Jr., W. A. Gallus Jr., I. Jankov, and R. W. Arritt, 2004: Convective contamination of model initializations and the poor forecasts that follow. *22nd Conf. on Severe Local Storms*, Hyannis, MA 17.8.

Davis, C. A., and M. L. Weisman, 1994: Balanced dynamics of mesoscale vortices produced in simulated convective systems. *J. Atmos. Sci.*, **51**, 2005–2030.

——, D. A. Ahijevych, and S. B. Trier, 2002: Detection and prediction of warm season midtropospheric vortices by the Rapid Update Cycle. *Mon. Wea. Rev.*, **130**, 24–42.

—— and S. B. Trier, 2002: Cloud-resolving simulations of mesoscale vortex intensification and its effect on a serial mesoscale convective system. *Mon. Wea. Rev.*, **130**, 2839–2858.

——, K. W. Manning, R. E. Carbone, S. B. Trier and J. D. Tuttle, 2003: Coherence of warm season continental rainfall in numerical weather prediction models. *Mon. Wea. Rev.*, **131**, 2667-2679.

——, N. Atkins, D. Bartels, L. Bosart, M. Coniglio, G. Bryan, W. Cotton, D. Dowell, B. Jewett, R. Johns, D. Jorgensen, J. Knievel, K. Knupp, W. Lee, G. Mcfarquhar, J. Moore, R. Przybylinski, R. Rauber, B. Smull, R. Trapp, S. Trier, R. Wakimoto, M. Weisman and C. Ziegler, 2004: The Bow Echo and MCV Experiment: Observations and opportunities. *Bull. Amer. Meteor. Soc*., **85**, 1075–1093.

——, B. Brown, and R. Bullock, 2006: Object-based verification of precipitation forecasts. Part II: Application to convective rain systems. *Mon. Wea. Rev.*, **134**, 1785–1795.

—— and S. B. Trier, 2007: Mesoscale convective vortices observed during BAMEX. Part I: Kinematic and thermodynamic structure. *Mon. Wea. Rev.*, **135**, 2029–2049.

—— and T. J. Galarneau, 2009: The vertical structure of mesoscale convective vortices. *J. Atmos. Sci.*, **66**, 686–704.

Done, J., C. A. Davis, and M. L. Weisman, 2004: The next generation of NWP: Explicit forecasts of convection using the Weather Research and Forecast (WRF) Model. *Atmos. Sci. Lett*., **5**, 110-117.

Doswell, C. A., and E. N. Rasmussen, 1994: The effect of neglecting the virtual temperature correction on CAPE calculations. Wea. Forecasting, **9**, 625–629.

Du, J., J. McQueen, G. J. DiMego, T. L. Black, H. Juang, E. Rogers, B. S. Ferrier, B. Zhou, Z. Toth, and S. Tracton, 2004: The NOAA/NWS/NCEP Short Range Ensemble Forecast (SREF) system: Evaluation of an initial condition vs multiple model physics ensemble approach. *Preprints, 20th Conference on Weather Analysis and Forecasting/ 16th Conference on Numerical Weather Prediction*, Seattle, WA, Amer. Meteor. Soc., CD-ROM, 21.3.

Dyer, A. J., and B. B. Hicks, 1970: Flux-gradient relationships in the constant flux layer. *Quart. J. Roy. Meteor. Soc*., **96**, 715-721.

Ek, M. B., K. E. Mitchell, Y. Lin, E. Rogers, P. Grunmann, V. Koren, G. Gayno, and J. D. Tarpley, 2003: Implementation of Noah Land Surface Model advances in the National Centers for Environmental Prediction operational mesoscale Eta Model, *J. Geophys. Res*., 108(D22), 8851, doi:10.1029/2002JD003296.

Ferrier, B. S., Y. Jin, Y. Lin, T. Black, E. Rogers, and G. DiMego, 2002: Implementation of a new grid-scale cloud and rainfall scheme in the NCEP Eta Model. Preprints, *15th Conf. On Numerical Weather Prediction*, San Antonio, TX, Amer. Meteor. Soc., 280-283.

Fritsch, J. M., R. Kane, and C. Chelius, 1986: The contribution of mesoscale convective weather systems to the warm-season precipitation in the United States. *J. Appl. Meteor.*, **25**, 1333–1345.

——, J. D. Murphy, and J. S. Kain, 1994: Warm-core vortex amplification over land. *J. Atmos. Sci*., **51**, 1780–1807.

——, and R.E. Carbone, 2004: Improving quantitative precipitation forecasts in the warm season: A USWRP research and development strategy. *Bull. Amer. Meteor. Soc.*, 85, 955–965.

Galarneau, T. J., L. F. Bosart, C. A. Davis, and R. McTaggart-Cowan, 2009: Baroclinic transition of a long-lived mesoscale convective vortex. *Mon. Wea. Rev.*, **137**, 562–584.

Germann, U., I. Zawadzki, and B. Turner, 2006: Predictability of precipitation from continental radar images. Part IV: Limits to prediction. *J. Atmos. Sci.*, **63**, 2092–2108.

Grell, G. A., and D. Devenyi, 2002: A generalized approach to parameterizing convection combining ensemble and data assimilation techniques. *Geophys. Res. Lett.,* **29,** 1693, doi: 10.1029/2002GL015311.

Hamill, T. M., and S. J. Colucci, 1997: Verification of Eta–RSM short-range ensemble forecasts. *Mon. Wea. Rev.*, **125**, 1312–1327.

——, and S. J. Colucci, 1998: Evaluation of Eta-RSM ensemble probabilistic precipitation forecasts. *Mon. Wea. Rev*., **126**, 711-724.

Harvey, L. O., K. R. Hammond, C. M. Lusk, and E. F. Mross, 1992: The application of signal detection theory to weather forecasting behavior. *Mon. Wea. Rev.*, **120**, 863–883.

Hawblitzel, D. P., F. Zhang, Z. Meng, and C. A. Davis, 2007: Probabilistic evaluation of the dynamics and predictability of the mesoscale convective vortex of 10–13 June 2003. *Mon. Wea. Rev.*, **135**, 1544–1563.

Hohenegger, C., and C. Schär, 2007: Atmospheric predictability at synoptic versus cloud-resolving scales. *Bull. Amer. Meteor. Soc.*, **88**, 1783–1793.

Hong, S.-Y, and J.-O. J. Lim, 2006: The WRF single-moment 6-class microphysics scheme (WSM6). *J. Korean Meteor. Soc.*, **42**, 129-151.

Janjic, Z. I., 1994: The step-mountain Eta coordinate model: Further developments of the convection, viscous sublayer, and turbulence closure schemes. *Mon. Wea. Rev*., **122**, 927-945.

——, 1996: The surface layer in the NCEP Eta Model. *11th Conf. on Numerical Weather Prediction*, Norfolk, VA, 19-23 August 1996; Amer. Meteor. Soc., Boston, MA, 354-355.

——, 2002: Nonsingular implementation of the Mellor-Yamada Level 2.5 Scheme in the NCEP Meso model. NCEP Office Note No. 437, NOAA/NWS, 61 pp.

——, 2003: A nonhydrostatic model based on a new approach. *Meteorol. Atmos. Phys*., 82, 271-285.

Johnson, R. H., and B. E. Mapes, 2001: Mesoscale processes and severe convective weather. C. A. Doswell III, Ed., AMS Monograph, *Severe Convective Weather*, 28, 71-122.

Johnston, E. C., 1982: Mesoscale vorticity centers induced by mesoscale convective complexes. Preprints, *Ninth Conf. On Weather Forecasting and Analysis*, Seattle, WA, Amer. Meteor. Soc., 196-200.

Kain, J. S., and J. M. Fritsch, 1993: Convective parameterization for mesoscale models: The Kain-Fritcsh scheme, *The representation of cumulus convection in numerical models*, K. A. Emanuel and D.J. Raymond, Eds., Amer. Meteor. Soc., 246 pp.

Kong, F., K. K. Droegemeier, and N. L. Hickmon, 2006: Multi-resolution ensemble forecasts of an observed tornadic thunderstorm system, Part I: Comparison of coarse and fine-grid experiments. *Mon. Wea. Rev*., **124**, 807-833.

——, ——, and ——, 2007: Multi-resolution ensemble forecasts of an observed tornadic thunderstorm system, Part II. Storm scale experiments. *Mon. Wea. Rev*., **135**, 759-782.

——, M. Xue, K. K. Droegemeier, D. Bright, M. C. Coniglio, K. W. Thomas, Y. Wang, D. Weber, J. S. Kain, S. J. Weiss, and J. Du, 2007: Preliminary analysis on the real-time storm-scale ensemble forecasts produced as a part of the NOAA Hazardous Weather Testbed 2007 Spring Experiment. *Preprints, 22nd Conference On Weather Analysis and Forecasting/18th Conference on Numerical Weather Prediction*, Park City, UT, Amer. Meteor. Soc., 3B.2.

——, M. Xue, K. W. Thomas, J. Gao, Y. Wang, K. Brewster, K. K. Droegemeier, J. Kain, S. Weiss, D. Bright, M. Coniglio, and J. Du, 2009: A realtime storm-scale ensemble forecast system: 2009 Spring Experiment. Preprints, *23rd Conference on Weather Analysis and Forecasting/19th Conference on Numerical Weather Prediction*, Omaha, NE, Amer. Meteor. Soc., 16A.3.

Lilly, D. K., 1990: Numerical prediction of thunderstorms – Has its time come? *Quart. J. Roy. Meteor. Soc*., **116**, 779-797.

Lorenz, E. N., 1969: The predictability of a flow which possesses many scales of motion. *Tellus*, **21**, 289-307.

Mason, I., 1982: A model for assessment of weather forecasts. *Aust. Met. Mag.*, **30**, 291-303.

Mellor, G. L., and T. Yamada, 1982: Development of a turbulence closure model for geophysical fluid problems. *Rev. Geophys.,* **20,** 851–875.

Menard, R. D., and J. Fritsch, 1989: A mesoscale convective complex-generated inertially stable warm core vortex. *Mon. Wea. Rev.*, **117**, 1237–1261.

Mlawer, E. J., S. J. Taubman, P. D. Brown, M. J. Iacono, and S. A. Clough, 1997: Radiative transfer for inhomogeneous atmosphere: RRTM, a validated correlated-k model for the long-wave. *J. Geophys. Res*., 102(D14), 16663-16682.

Molinari, J., and M. Dudek, 1992: Parameterization of convective precipitation in mesoscale numerical models: A Critical Review. *Mon. Wea. Rev*., **120**, 326–344.

Monin, A.S. and A.M. Obukhov, 1954: Basic laws of turbulent mixing in the surface layer of the atmosphere. *Contrib. Geophys. Inst. Acad. Sci*. USSR, (151), 163-187 (in Russian).

Mylne, K. R., 1999: The use of forecast value calculations for optimal decision making using probability forecasts. Preprints, *17th Conf. on Weather Analysis and Forecasting*, Denver, CO, Amer. Meteor. Soc., 235-239.

Noh, Y., W. G. Cheon, S.-Y. Hong, and S. Raasch, 2003: Improvement of the K-profile model for the planetary boundary layer based on large eddy simulation data. *Boundary Layer Meteor*., **107**, 401-427.

Paulson, C. A., 1970: The mathematical representation of wind speed and temperature profiles in the unstable atmospheric surface layer. *J. Appl. Meteor.*, **9**, 857-861.

Raymond, D. J., and H. Jiang, 1990: A theory for long-lived mesoscale convective systems. *J. Atmos. Sci.*, **47**, 3067–3077.

Richardson, D. S., 2000: Applications of cost-loss models. Proc. *Seventh ECMWF Workshop on Meteorological Operational Systems*, Reading, United Kingdom, ECMWF, 209-213.

——, 2001: Measures of skill and value of ensemble prediction systems, their interrelationship and the effect of ensemble size. *Quart. J. Roy. Meteor. Soc.,* **127**, 2473-2489.

Robinson, G. D., 1967: Some current projects for global meteorological observation and experiment. *Quart. J. Roy. Meteor. Soc*., **93**, 409-418.

Rogers, R. F., and J. M. Fritsch, 2001: Surface cyclogenesis from convectively driven amplification of midlevel mesoscale convective vortices. *Mon. Wea. Rev.*, **129**, 605–637.

Schumacher, R. S., and R. H. Johnson, 2006: Characteristics of U.S. extreme rain events during 1999–2003. *Wea. Forecasting*, **21**, 69–85.

—— and ——, 2009: Quasi-stationary, extreme-rain-producing convective systems associated with midlevel cyclonic circulations. *Wea. Forecasting*, **24**, 555–574.

Schwartz, C. S., J. S. Kain, S. J. Weiss, M. Xue, D. R. Bright, F. Kong, K. W. Thomas, J. J. Levit, M. C. Coniglio, Matthew S. Wandishin, 2009: Toward improved convection-allowing ensembles: Model physics sensitivities and optimizing probabilistic guidance with small ensemble membership. *Wea. Forecasting* (In Press).

Skamarock, W. C., M. L. Weisman, and J. B. Klemp, 1994: Three-dimensional evolution of simulated long-lived squall lines. *J. Atmos. Sci.*, **51**, 2563–2584.

——, J. B. Klemp, J. Dudhia, D. O. Gill, D. M. Barker, W. Wang and J. G. Powers, 2005: A description of the Advanced Research WRF Version 2, NCAR Tech Note, NCAR/TN–468+STR, 88 pp. [Available from UCAR Communications, P.O. Box 3000, Boulder, CO, 80307]. Also available at: http://box.mmm.ucar.edu/wrf/users/docs/arw_v2.pdf

Smagorinsky, J., 1969: Problems and promises of deterministic extended range forecasting. *Bull. Amer. Meteor. Soc*., **50**, 286-311.

Thompson, G., R. M. Rasmussen, and K. Manning, 2004: Explicit forecasts of winter precipitation using an improved bulk microphysics scheme. Part I: Description and sensitivity analysis. *Mon. Wea. Rev*., **132**, 519–542.

Toth, Z., and E. Kalnay, 1993: Ensemble forecasting at NMC: The generation of perturbations. *Bull. Amer. Meteor. Soc*., **74**, 2317-2330.

——, and E. Kalnay, 1997: Ensemble forecasting at NCEP and the breeding method. *Mon. Wea. Rev*., **125**, 3297-3319.

Trier, S. B., C. A. Davis, and J. D. Tuttle, 2000a: Long-lived mesoconvective vortices and their environment. Part I: Observations from the central United States during the 1998 warm season. *Mon. Wea. Rev.*, **128**, 3376–3395.

——, ——, and W. C. Skamarock, 2000b: Long-lived mesoconvective vortices and their environment. Part II: Induced thermodynamic destabilization in idealized simulations. *Mon. Wea. Rev*., **128**, 3396–3412.

——, and C. A. Davis, 2002: Influence of balanced motions on heavy precipitation within a long-lived convectively generated vortex. *Mon. Wea. Rev.*, **130**, 877–899.

Wandishin, M., D. J. Stensrud, S. L. Mullen, and L. J. Wicker, 2008: On the predictability of mesoscale convective systems: Two-dimensional simulations. *Wea. Forecasting*, **23**, 773–785.

Webb, E. K., 1970: Profile relationships: the log-linear range and extension to strong stability. *Quart. J. Roy. Meteor. Soc.,* **96**, 67–90.

Weisman, M. L., C. Davis, W. Wang, K. W. Manning, and J. B. Klemp, 2008: Experiences with 0–36-h explicit convective forecasts with the WRF-ARW model. *Wea. Forecasting*, **23**, 407–437.

Xue, M., K. K. Droegemeier, V. Wong, A. Shapiro, K. Brewster, F. Carr, D. Weber, Y. Liu, and D.-H. Wang, 2001: The Advanced Regional Prediction System (ARPS) – A multiscale nonhydrostatic atmospheric simulation and prediction tool. Part II: Model physics and applications. *Meteor Atmos. Phys*., **76**, 143-165.

Xue, M., F. Kong, D. Weber, K. W. Thomas, Y. Wang, K. Brewster, K. K. Droegemeier, J. S. Kain, S. J. Weiss, D. Bright, M. Wandishin, M. Coniglio, and J. Du, 2007: CAPS realtime storm-scale ensemble and high-resolution forecasts as part of the NOAA Hazardous Weather Testbed 2007 Spring Experiment. *Preprints, 22nd Conference On Weather Analysis and Forecasting/18th Conference on Numerical Weather Prediction*, Park City, UT, Amer. Meteor. Soc., 3B.1.

——, F. Kong, K. W. Thomas, J. Gao, Y. Wang, K. Brewster, K. K. Droegemeier, X. Wang, J. S. Kain, S. J. Weiss, D. R. Bright, M. C. Coniglio, and J. Du, 2009: CAPS realtime multi-model convection-allowing ensemble and 1-km convection-resolving forecasts for the NOAA Hazardous Weather Testbed 2009 Spring Experiment. Preprints, *23rd Conference on Weather Analysis and Forecasting/19th Conference on Numerical Weather Prediction*, Omaha, NE, Amer. Meteor. Soc., 16A.2.

Zhang, D. L., and J. M. Fritsch, 1987: Numerical simulation of the meso-β scale structure and evolution of the 1977 Johnstown Flood. Part II: Inertially stable warm-core vortex and the mesoscale convective complex. *J. Atmos. Sci.*, **44**, 2593–2612.

Zhang, F., A. M. Odins, and J. W. Nielsen-Gammon, 2006: Mesoscale predictability of an extreme warm-season precipitation event. *Wea. Forecasting*, **21**, 149-166.

List of Figures

Figure 1 Domains for a) NCEP SREF ensemble members and b) ENS4 and ENS20 ensemble members.

Figure 2 RUC analyses of 500-hPa absolute vorticity (10^5 s^{-1}; shaded), geopotential height (m; contours), and wind speeds greater than 15 ms^{-1} (hatched) valid 1200 UTC a) 28 May, b) May

29, c) 30 May, c) 31 May, and d) 01 June, 2007. f) RUC analysis of maximum 600-hPa potential vorticity (PVU; shaded) for the period 0900 - 2200 UTC 01 June 2007. The approximate path of the MCV is indicated by the curved black arrow in f).

Figure 3 Radar reflectivity "snapshots" of an MCV-producing MCS at different times indicated above or below each snapshop. The track of the MCV as inferred from composite radar reflectivity is indicated by the black/grey dots connected by the black line. Black (grey) dots indicate the location of the MCV at times reflectivity is not (is) pictured. RUC analyses of 300-hPa wind direction (magnitude; ms^{-1}) at 1500 UTC 01 June 2007 is shown by vectors (shading). Locations of tornado (red triangles), hail (blue squares), and wind reports (green circles) that occurred 1700 – 2200 UTC are marked.

Figure 4 Vertical cross sections from RUC analyses of potential temperature (contours) and potential vorticity (shaded) at a) 0900 UTC, b) 1500 UTC, c) 1800 UTC, and d) 2100 UTC, 01 June 2007. The locations of the cross-sections in a)-d) are indicated in f) along with the maximum 600-hPa potential vorticity during the period 0900-2200 UTC 01 June. e) time-height section of potential temperature and potential vorticity averaged over approximately 300-km centered over the mid-lower tropospheric PV anomaly. Times at which the cross sections in a)-d) are valid are indicated by the vertical lines in e) and locations of all the cross sections used to create e) are indicated in f).

Figure 5 Magnitude of the 10-m to 700-hPa shear vector (WSHR; ms^{-1} contours), most unstable convective available potential energy (MUCAPE; Jkg^{-1} shaded), and 10-m winds (grey wind barbs; ms^{-1}) from a) the RUC analysis valid at 1800 UTC 01 June 2007, and c) the 18 h forecast from the NAM model initialized at 0000 UTC 01 June 2007. 600-hPa relative vorticity (s^{-1}; shaded), geopotential height (m; contours), wind vectors, and wind speeds greater than 20 ms^{-1} (hatched) from b) the RUC analysis and d) the NAM, valid at the same times as in a) and c), respectively. The arcing dashed lines in a) and b) denote the location of the observed convective line.

Figure 6 Forecasts (21 h lead time) of 600-hPa relative vorticity (shaded), geopotential height (contours), and 600-hPa wind speed greater than 20 ms^{-1} (hatched) for (a)-(e) ENS4, and (f)-(t) ENS20 ensemble members valid at 1800 UTC 01 June 2007. Forecast probabilities of 600-hPa wind speed greater than 20 ms^{-1} (shaded), ensemble mean 600-hPa geopotential height (contours), and RUC analyses of wind speed greater than 20 ms^{-1} (hatched) for (u) ENS4, (v) ENS20, (w) $ENS20_{BMJ}$, (x) $ENS20_{KF}$, (y) $ENS20_{GD}$. ROC scores for the 20 ms^{-1} 600-hPa wind speed threshold are indicated at the bottom-right of (u)-(y).

Figure 7 Same as Figure 6 except (a)-(e) are for $ENS4^{phys}$ and (f)-(t) are for $ENS20^{phys}$, and (u) $ENS4^{phys}$, (v) $ENS20^{phys}$, (w) $ENS20^{phys}{}_{BMJ}$, (x) $ENS20^{phys}{}_{KF}$, and (y) $ENS20^{phys}{}_{GD}$.

Figure 8 21-h forecasts of MUCAPE (shaded), magnitude of the 10-m to 700 hPa shear vector (WSHR; ms^{-1} contours), and 10-m winds (barbs) for (a)-(e) ENS4, and (f)-(t) ENS20 ensemble members. Forecast probabilities (shaded) and RUC analyses (hatched) of WSHR greater than 16 ms^{-1} for (u) ENS4, (v) ENS20, (w) $ENS20_{bmj}$, (x) $ENS20_{kf}$, (y) $ENS20_{GD}$. (z) – (δ) same as (u) – (y) except for MUCAPE greater than 1000 Jkg^{-1}. ROC scores (see text for descriptions) are indicated at the top-right of (u) – (δ).

Figure 9 Same as Figure 8 except for $ENS4^{phys}$ and $ENS20^{phys}$ subsets.

Figure 10 Manually identified MCV tracks for a) ENS20 (thin grey), ENS4 (thick black), and the RUC analysis (grey line with black dots), and b) $ENS20^{phys}$ (thin grey), $ENS4^{phys}$ (thick black), and the RUC analysis (grey line with black dots). Triangles mark the location of MCVs at forecast hour 18, and average displacement errors for various ensemble subsets at forecast hour 18 are shown in the bottom right of a) and b).

Figure 11 Time-height averages of vorticity budget terms in the RUC analyses: a) vorticity tendency [LHS of Eq. (3)], b) sum of the RHS terms in Eq. (3), c) vortex stretching, d) eddy flux (or vorticity advection), e) tilting, and f) vorticity.

Figure 12 Same as Figure 11, except for ENS20 ensemble member 02.

Figure 13 Same as Figure 11, except for ENS20^{phys} ensemble member 27.

Figure 14 Same as Figure 11, except for ENS4 ensemble member p1.

Figure 15 The sum of stretching, eddy flux, and tilting tendency terms for points in time-height space in which the sum of all three tendency terms is positive (gray shaded bars) and negative (black outlined bars) for members in a) – e) ENS4, f) – j) ENS20$_{BMJ}$, k) – o) ENS20$_{KF}$, p) – t) ENS20$_{GD}$, and u) RUC analyses. For the sum of positive (negative) tendencies, the values to the right of zero are positive (negative), so that right of zero always indicates which tendencies contribute most to either positive or negative sums. Spatial correlation coefficients in time-height space between vorticity tendency [LHS of Eq. (3)] and the sum of tendency terms (RHS of Eq. (3)] are indicated at the bottom right of each panel.

Figure 16 Same as Figure 15 except for a) – e) ENS4^{phys}, f) – j) ENS20$^{phys}_{BMJ}$, k) – o) ENS20$^{phys}_{KF}$, and p) – t) ENS20$^{phys}_{GD}$.

Figure 17 Time series of the maximum vorticity between 900- and 300-hPa for ensemble members in a) ENS4 and ENS4^{phys}, b) ENS20 subsets, and c) ENS20^{phys} subsets, and d) - f) same as a) -c) except for time series of the vertical level at which the maximum vorticity occurred. a) - f) also contain time series from the RUC analysis.

Figure 18 Time series of vortex stretching tendencies in ENS4^{phys} members and RUC analyses averaged over a) 600- to 400-hPa, b) 800- to 600-hPa, and c) 900- to 800-hPa. d) – f) same as a) – c) except for ENS20^{phys} members.

List of Tables

Table 1 ENS4 ensemble member specifications. NAMa and NAMf indicate NAM forecasts and analyses, respectively; em_pert and nmm_pert are perturbations from different SREF members; and em_n1, em_p1, nmm_n1, and nmm_p1 are different SREF members that are used for LBCs. The remaining table elements are described in the text.

Table 2 Same as Table 1 except for ENS4^{phys} ensemble member specifications.

Table 3 ENS20 ensemble member specifications. The members are grouped into 5-member subsets that have the same cumulus parameterizations. The ICs/LBCs table elements represent various SREF members and the remaining table elements are described in the text.

Table 4 Same as Table 3 except for ENS20^{phys} ensemble member specifications.

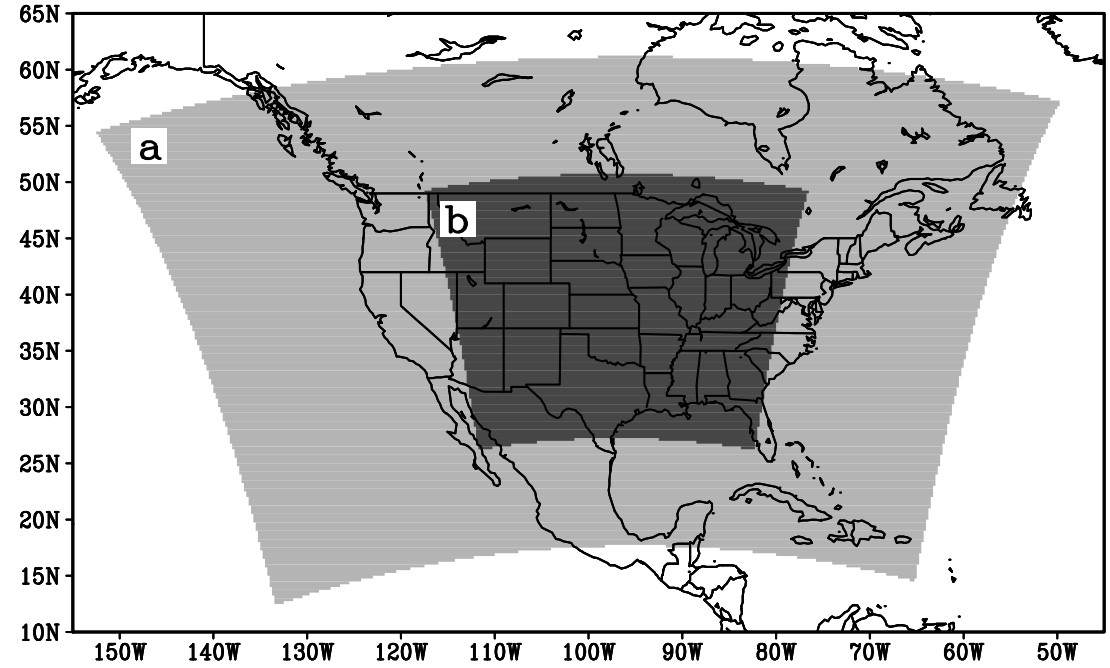

Figure 1 Domains for a) NCEP SREF ensemble members and b) ENS4 and ENS20 ensemble members.

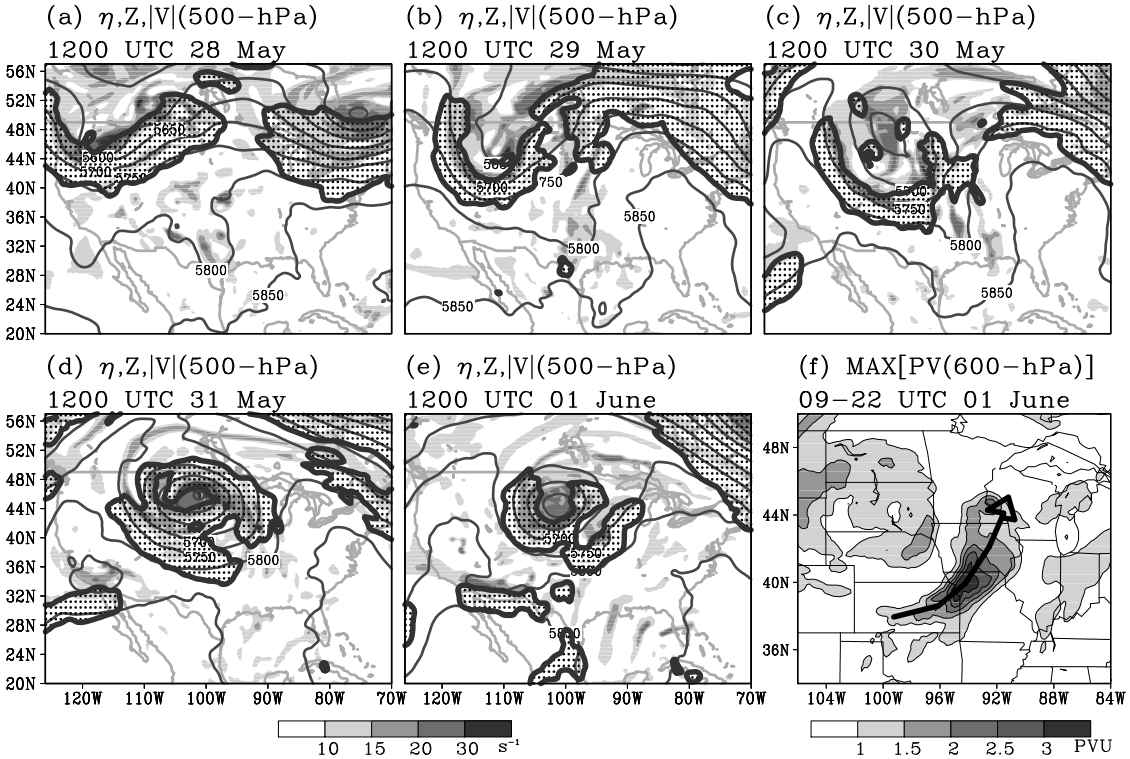

Figure 2 RUC analyses of 500-hPa absolute vorticity (10^5 s^{-1}; shaded), geopotential height (m; contours), and wind speeds greater than 15 ms^{-1} (hatched) valid 1200 UTC a) 28 May, b) May 29, c) 30 May, c) 31 May, and d) 01 June, 2007. f) RUC analysis of maximum 600-hPa potential vorticity (PVU; shaded) for the period 0900 - 2200 UTC 01 June 2007. The approximate path of the MCV is indicated by the curved black

arrow in f).

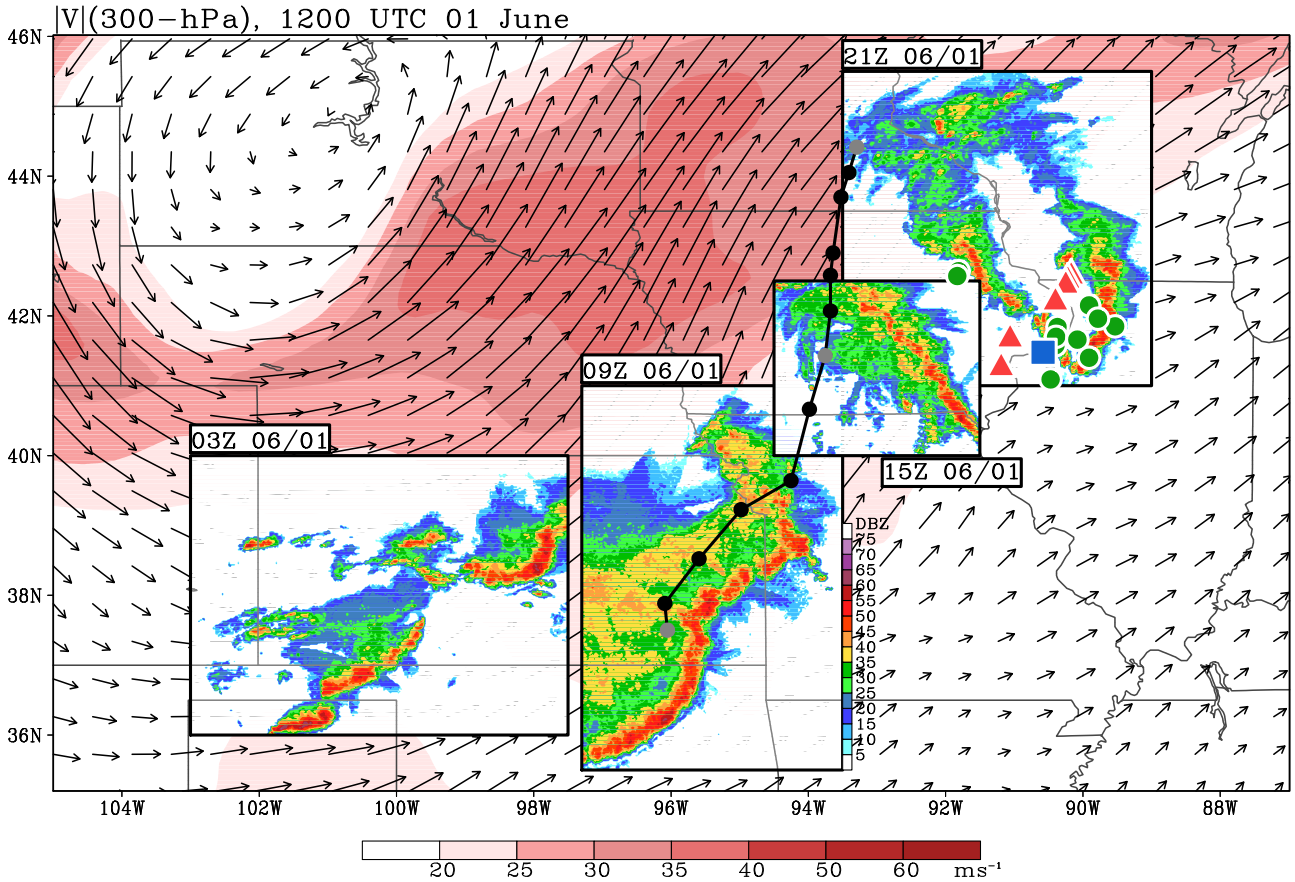

Figure 3 Radar reflectivity "snapshots" of an MCV-producing MCS at different times indicated above or below each snapshop. The track of the MCV as inferred from composite radar reflectivity is indicated by the black/grey dots connected by the black line. Black (grey) dots indicate the location of the MCV at times reflectivity is not (is) pictured. RUC analyses of 300-hPa wind direction (magnitude; ms^{-1}) at 1500 UTC 01 June 2007 is shown by vectors (shading). Locations of tornado (red triangles), hail (blue squares), and wind reports (green circles) that occurred 1700 – 2200 UTC are marked.

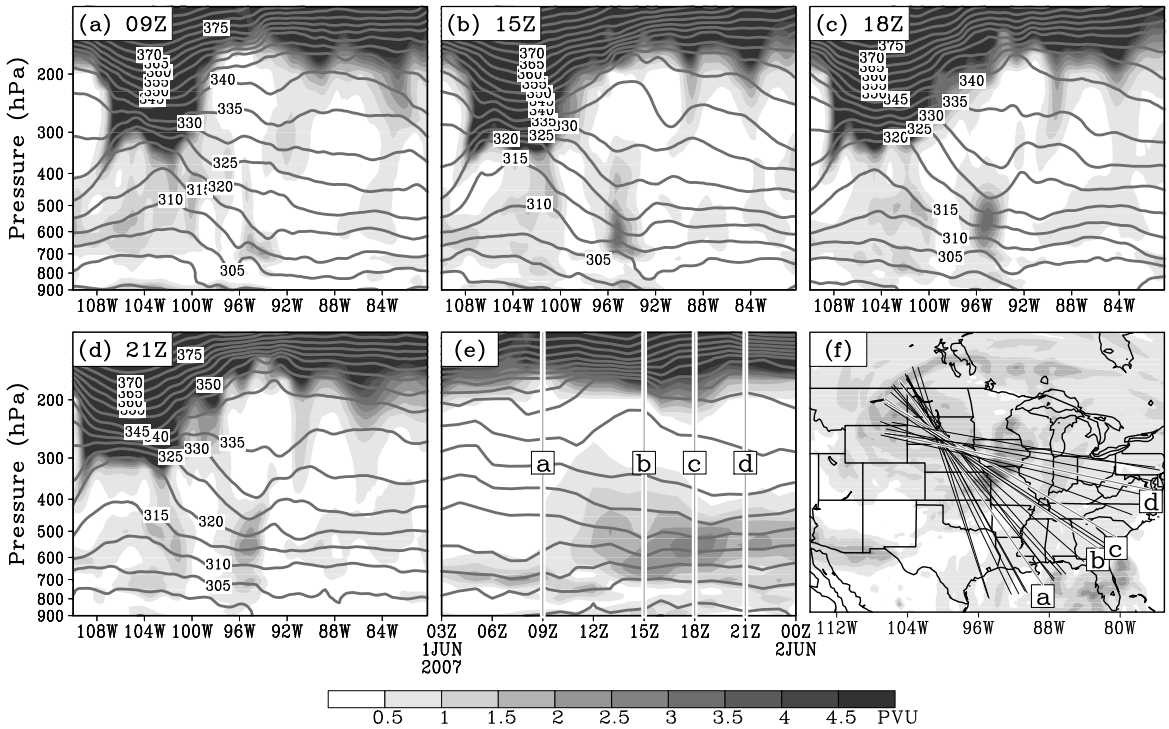

Figure 4 Vertical cross sections from RUC analyses of potential temperature (contours) and potential vorticity (shaded) at a) 0900 UTC, b) 1500 UTC, c) 1800 UTC, and d) 2100 UTC, 01 June 2007. The locations of the cross-sections in a)-d) are indicated in f) along with the maximum 600-hPa potential vorticity during the period 0900-2200 UTC 01 June. e) time-height section of potential temperature and potential vorticity averaged over approximately 300-km centered over the mid-lower tropospheric PV anomaly. Times at which the cross sections in a)-d) are valid are indicated by the vertical lines in e) and locations of all the cross sections used to create e) are indicated in f).

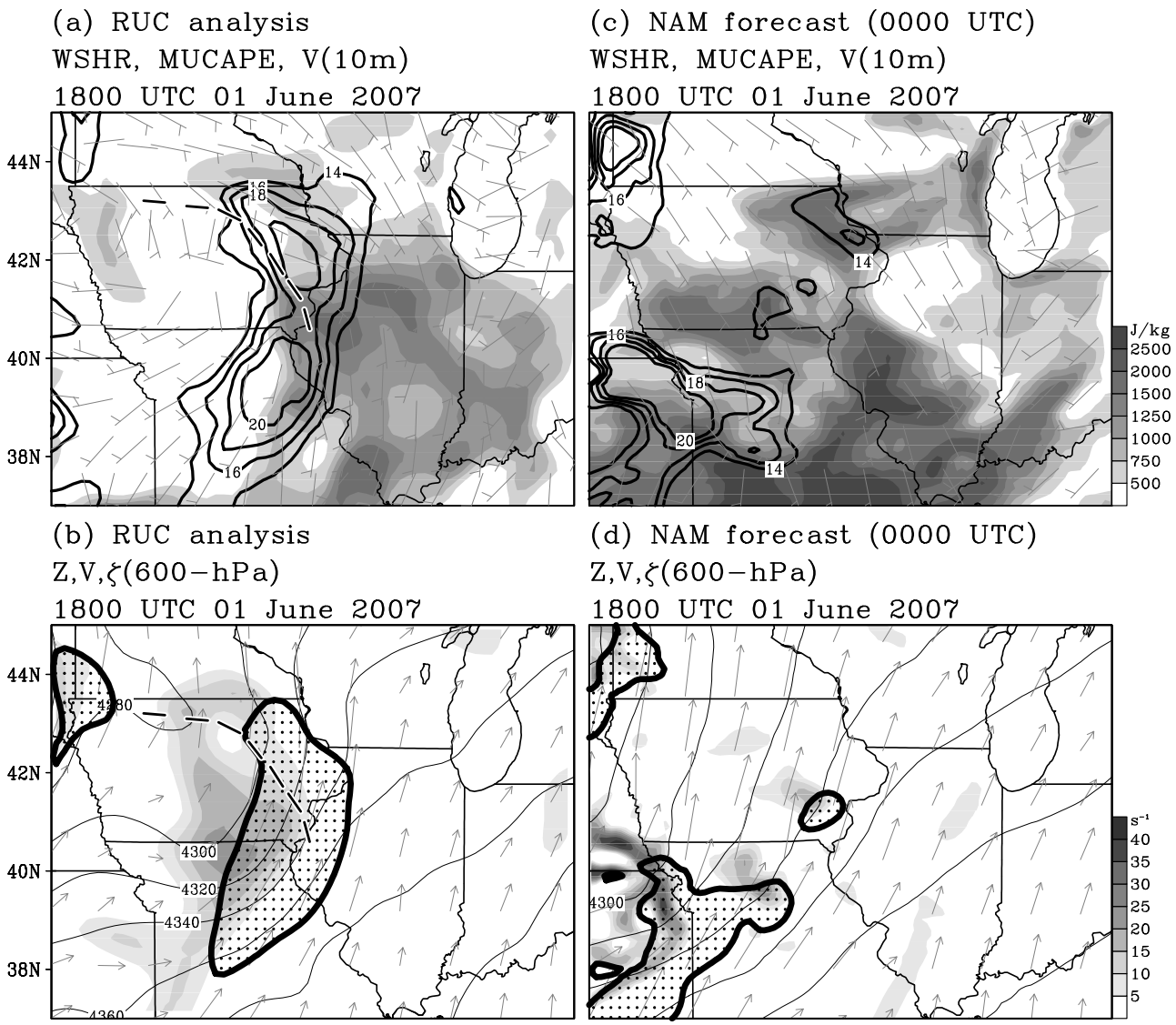

Figure 5 Magnitude of the 10-m to 700-hPa shear vector (WSHR; ms^{-1} contours), most unstable convective available potential energy (MUCAPE; Jkg^{-1} shaded), and 10-m winds (grey wind barbs; ms^{-1}) from a) the RUC analysis valid at 1800 UTC 01 June 2007, and c) the 18 h forecast from the NAM model initialized at 0000 UTC 01 June 2007. 600-hPa relative vorticity (s^{-1}; shaded), geopotential height (m; contours), wind vectors, and wind speeds greater than 20 ms^{-1} (hatched) from b) the RUC analysis and d) the NAM, valid at the same times as in a) and c), respectively. The arcing dashed lines in a) and b) denote the location of the observed convective line.

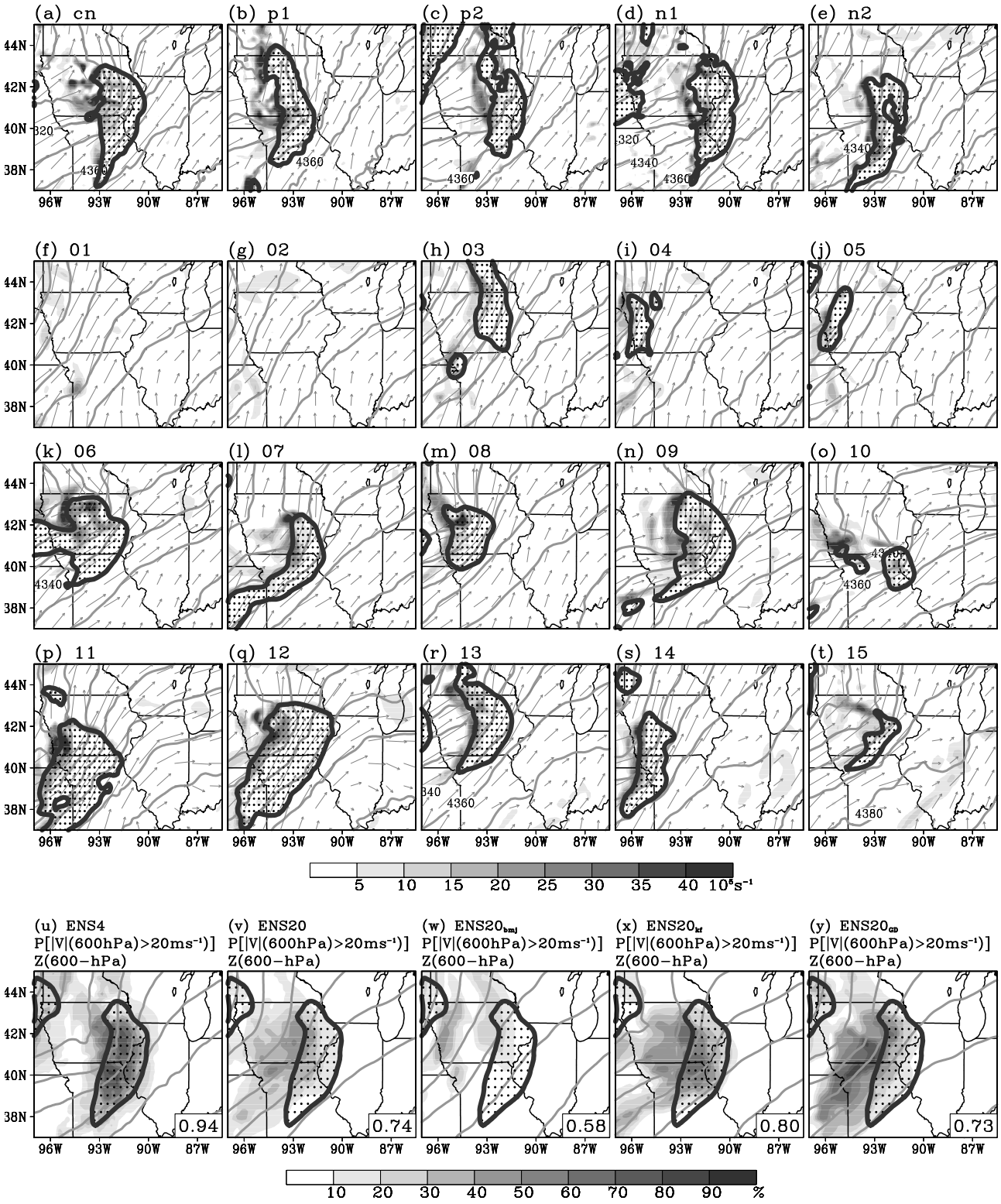

Figure 6 Forecasts (21 h lead time) of 600-hPa relative vorticity (shaded), geopotential height (contours), and 600-hPa wind speed greater than 20 ms^{-1} (hatched) for (a)-(e) ENS4, and (f)-(t) ENS20 ensemble members valid at 1800 UTC 01 June 2007. Forecast probabilities of 600-hPa wind speed greater than 20 ms^{-1} (shaded), ensemble mean 600-hPa geopotential height (contours), and RUC analyses of wind speed greater than 20 ms^{-1} (hatched) for (u) ENS4, (v) ENS20, (w) $ENS20_{BMJ}$, (x) $ENS20_{KF}$, (y) $ENS20_{GD}$. ROC scores for the 20 ms^{-1} 600-hPa wind speed threshold are indicated at the bottom-right of (u)-(y).

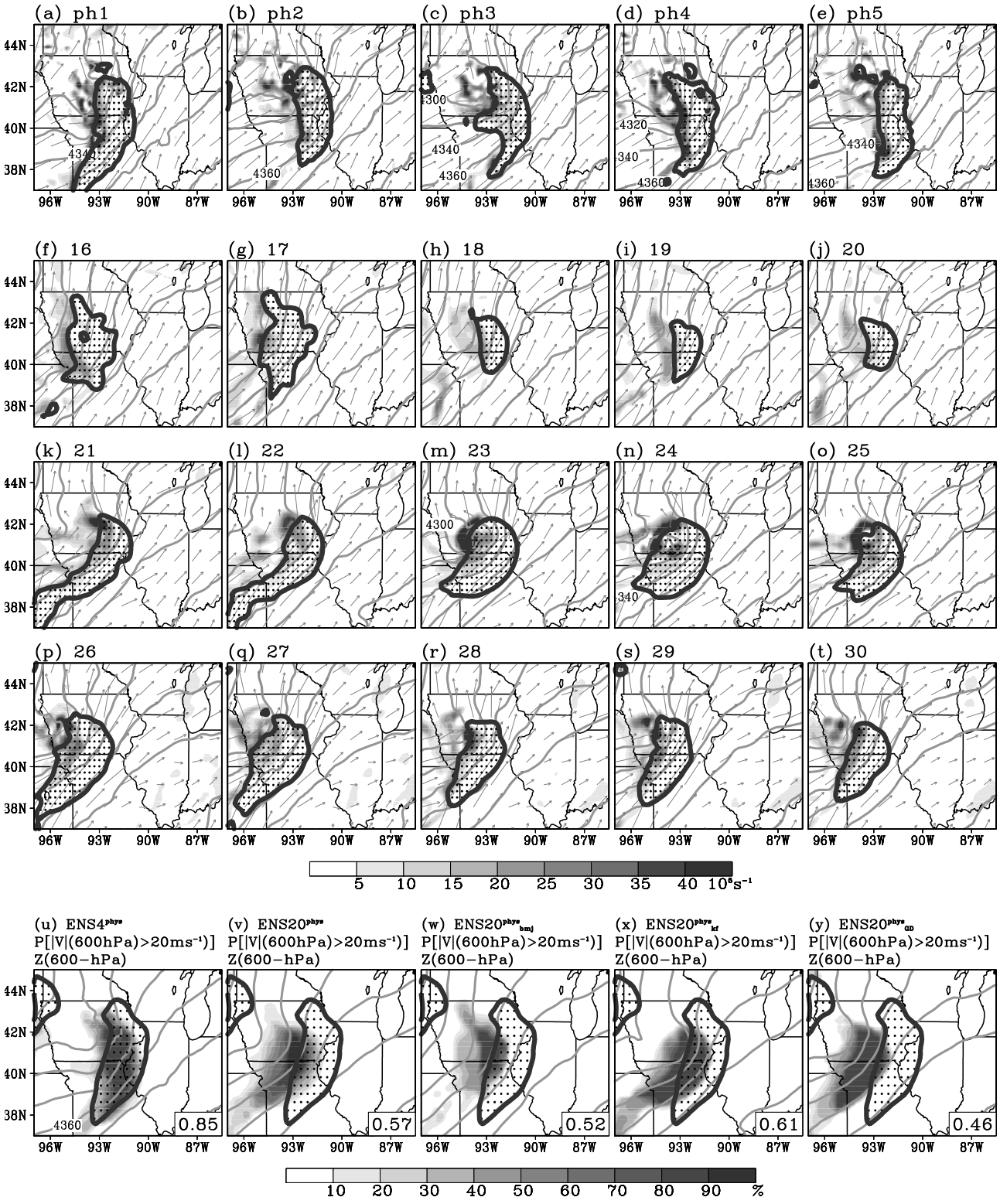

Figure 7 Same as Fig. 6 except (a)-(e) are for ENS4^{phys} and (f)-(t) are for ENS20^{phys}, and (u) ENS4^{phys}, (v) ENS20^{phys}, (w) ENS20$^{phys}{}_{BMJ}$, (x) ENS20$^{phys}{}_{KF}$, and (y) ENS20$^{phys}{}_{GD}$.

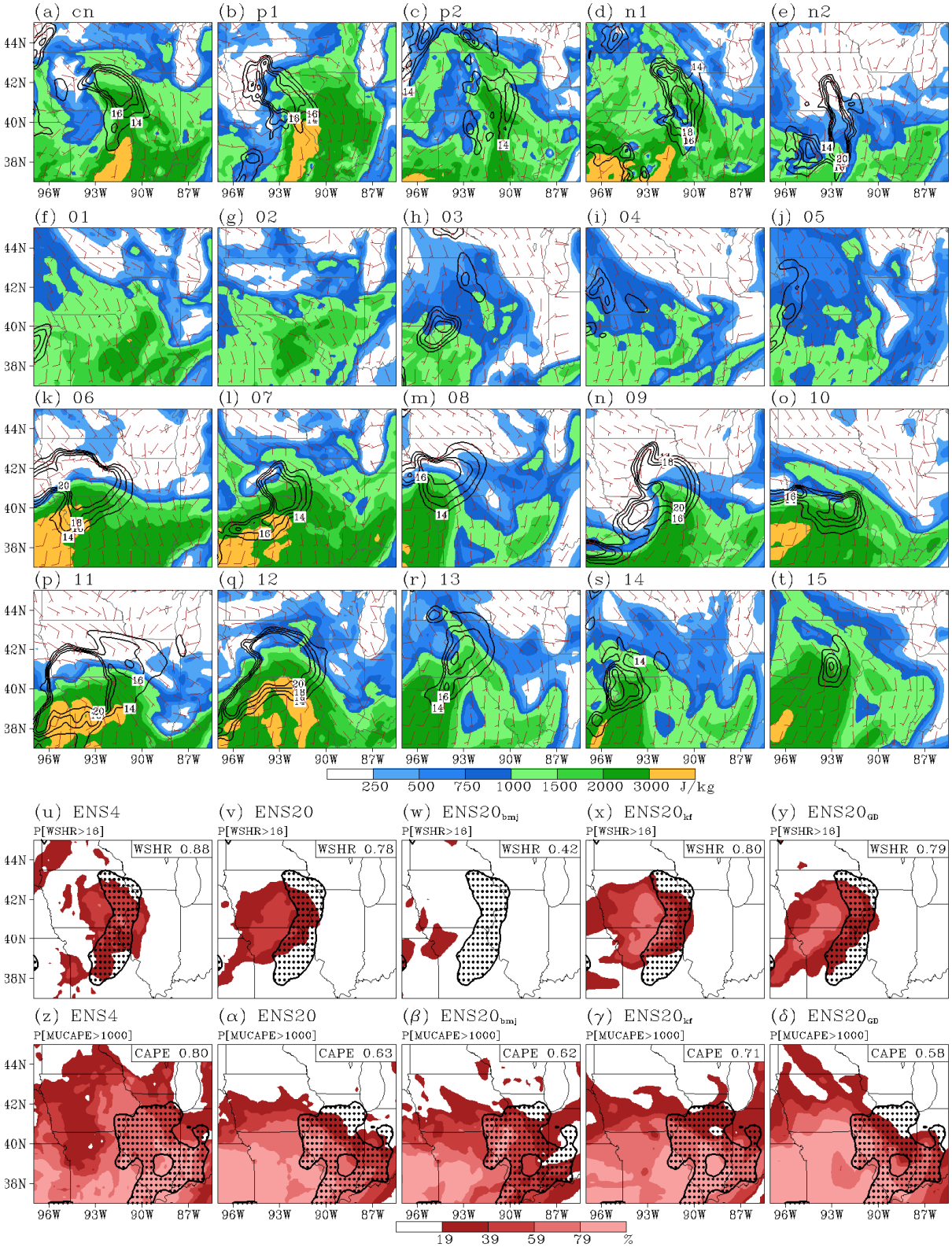

Figure 8 21-h forecasts of MUCAPE (shaded), magnitude of the 10-m to 700 hPa shear vector (WSHR; ms^{-1} contours), and 10-m winds (barbs) for (a)-(e) ENS4, and (f)-(t) ENS20 ensemble members. Forecast probabilities (shaded) and RUC analyses (hatched) of WSHR greater than 16 ms^{-1} for (u) ENS4, (v) ENS20, (w) $ENS20_{bmj}$, (x) $ENS20_{kf}$, (y) $ENS20_{GD}$. (z) – (δ) same as (u) – (y) except for MUCAPE greater than 1000 Jkg^{-1}. ROC scores (see text for descriptions) are indicated at the top-right of (u) – (δ).

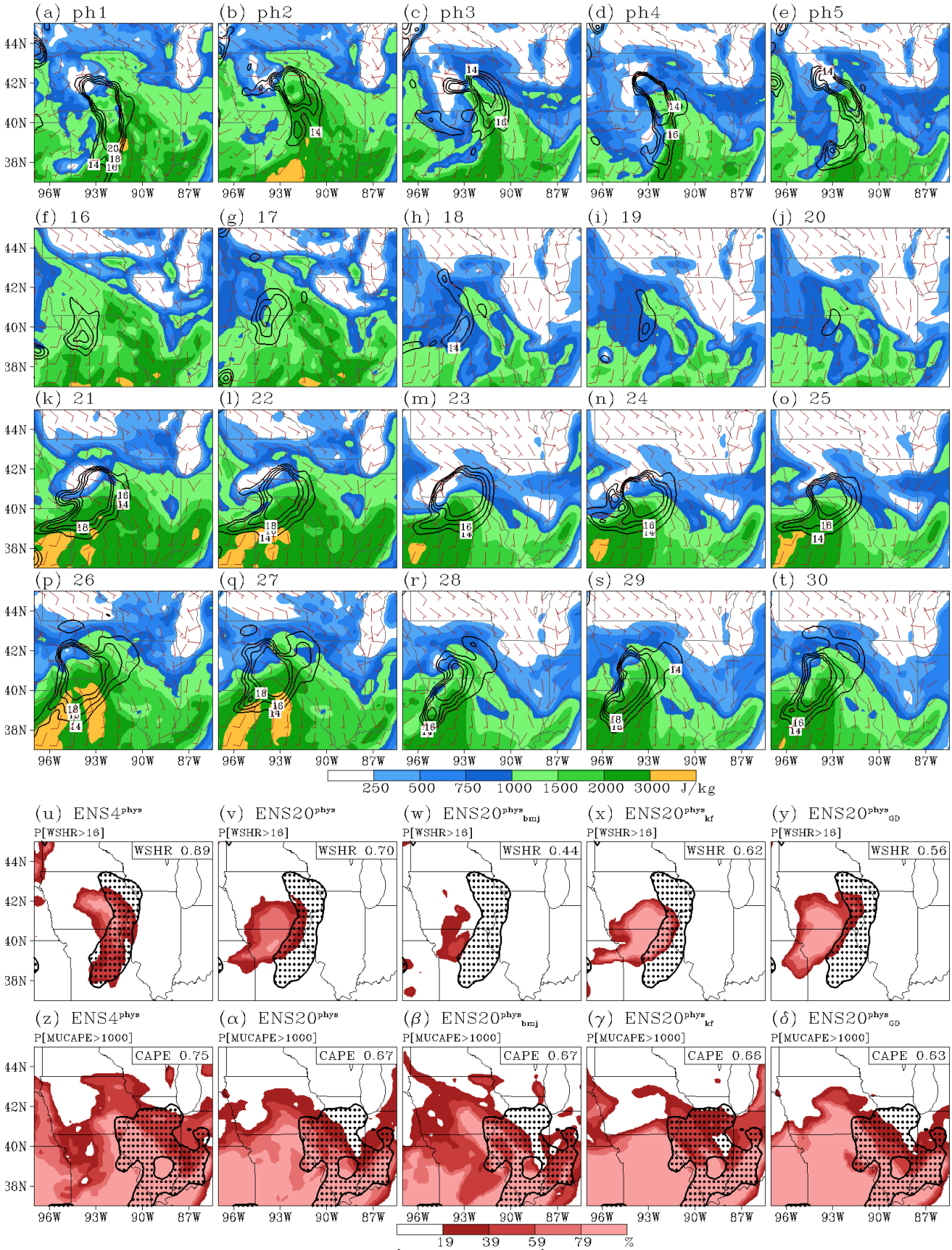

Figure 9 Same as Fig. 8 except for ENS4^{phys} and ENS20^{phys} subsets.

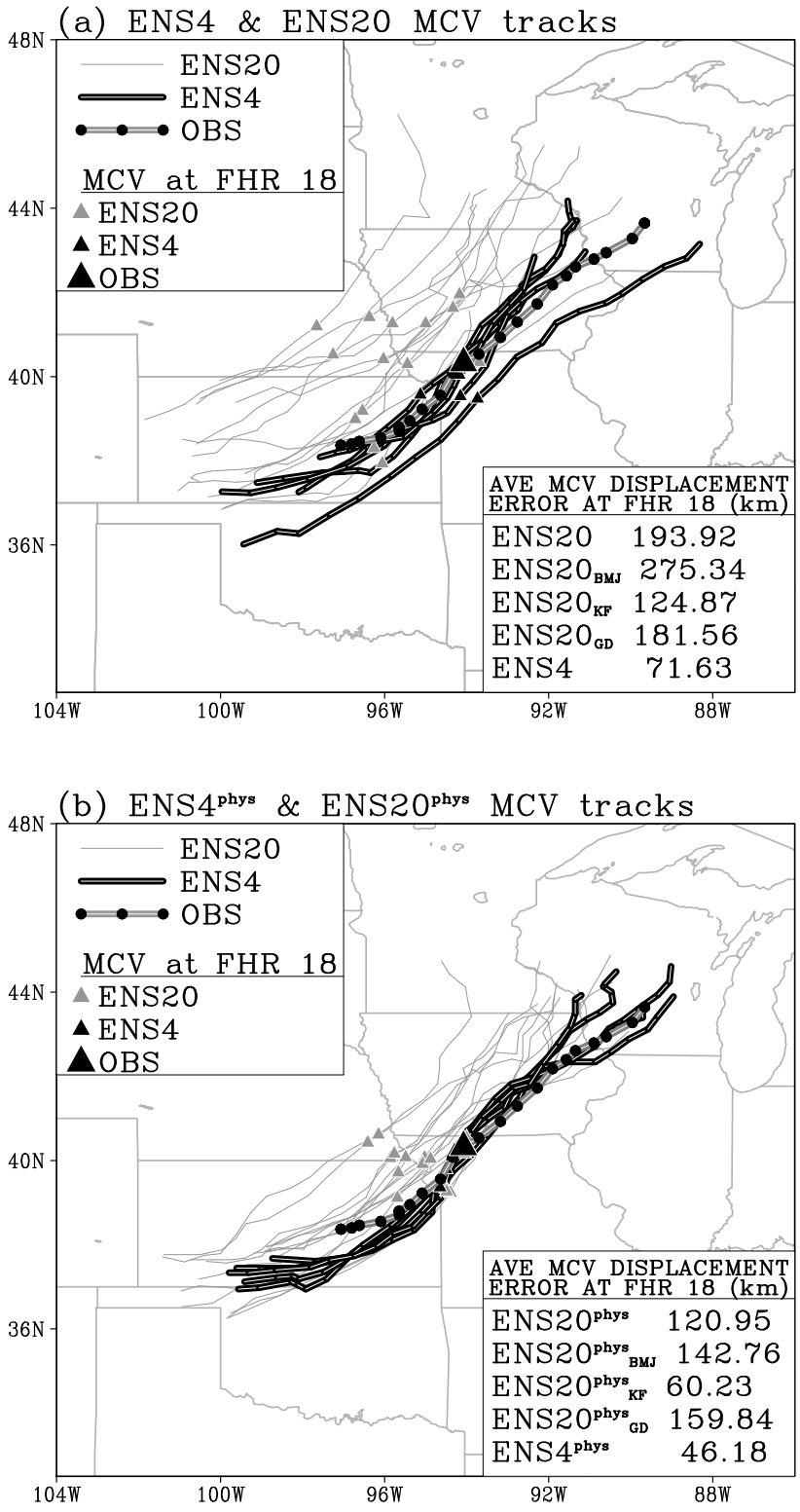

Figure 10 Manually identified MCV tracks for a) ENS20 (thin grey), ENS4 (thick black), and the RUC analysis (grey line with black dots), and b) ENS20^{phys} (thin grey), ENS4^{phys} (thick black), and the RUC analysis (grey line with black dots). Triangles mark the location of MCVs at forecast hour 18, and average displacement errors for various ensemble subsets at forecast hour 18 are shown in the bottom right of a) and b).

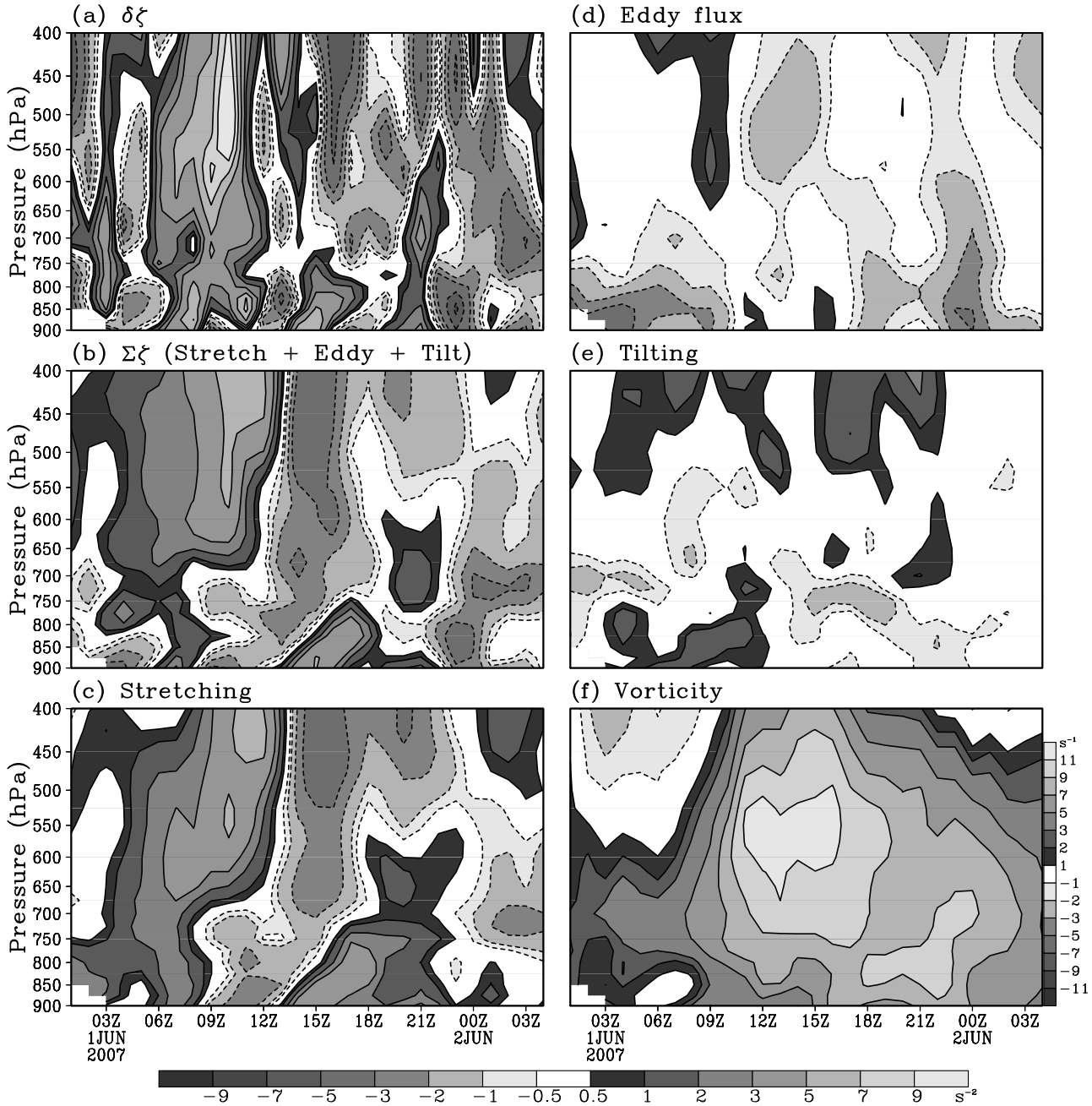

Figure 11 Time-height averages of vorticity budget terms in the RUC analyses: a) vorticity tendency [LHS of Eq. (3)], b) sum of the RHS terms in Eq. (3), c) vortex stretching, d) eddy flux (or vorticity advection), e) tilting, and f) vorticity.

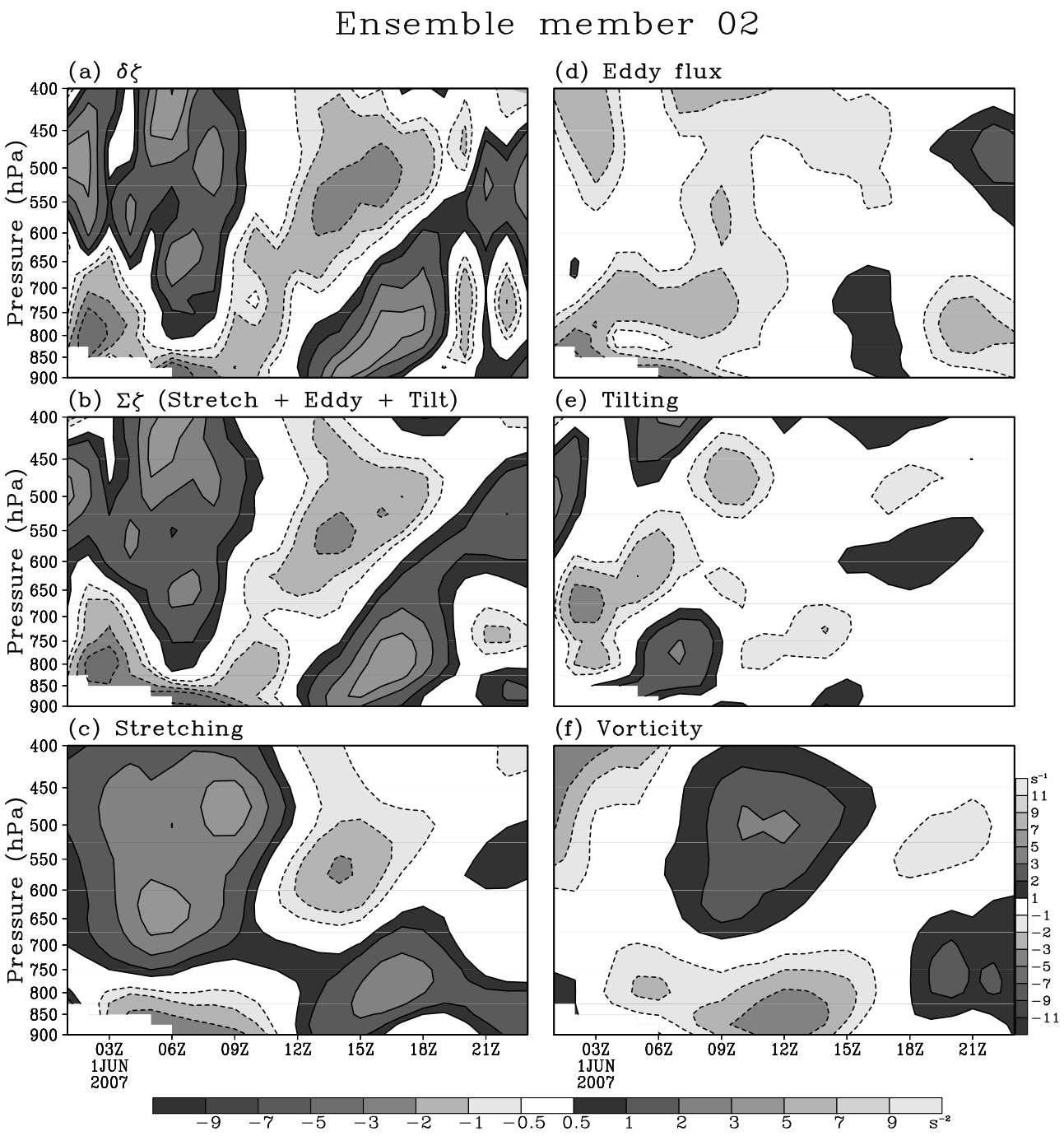

Figure 12 Same as Figure 11, except for ENS20 ensemble member 02.

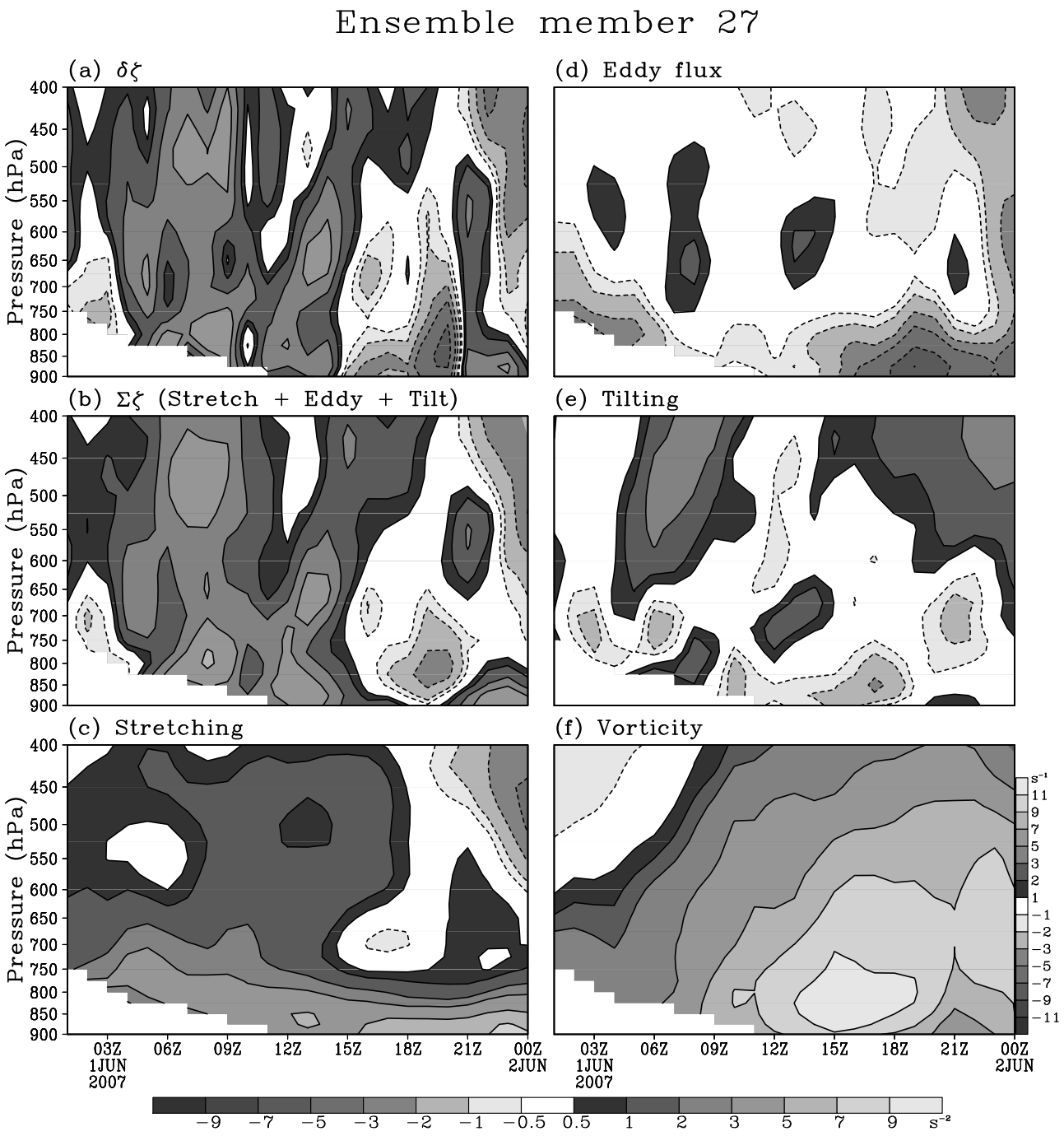

Figure 13 Same as Figure 11, except for ENS20^{phys} ensemble member 27.

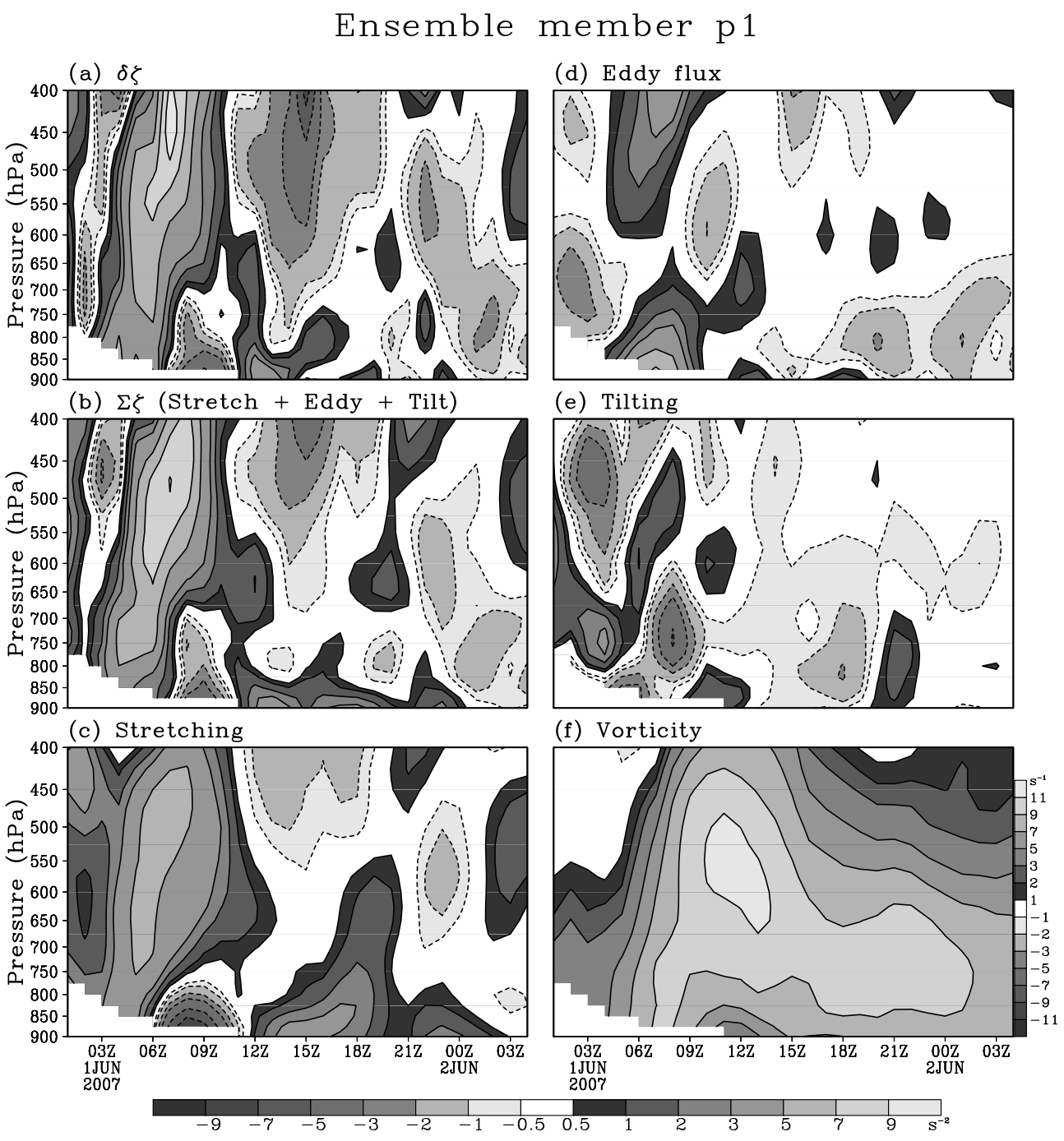

Figure 14 Same as Figure 11, except for ENS4 ensemble member p1.

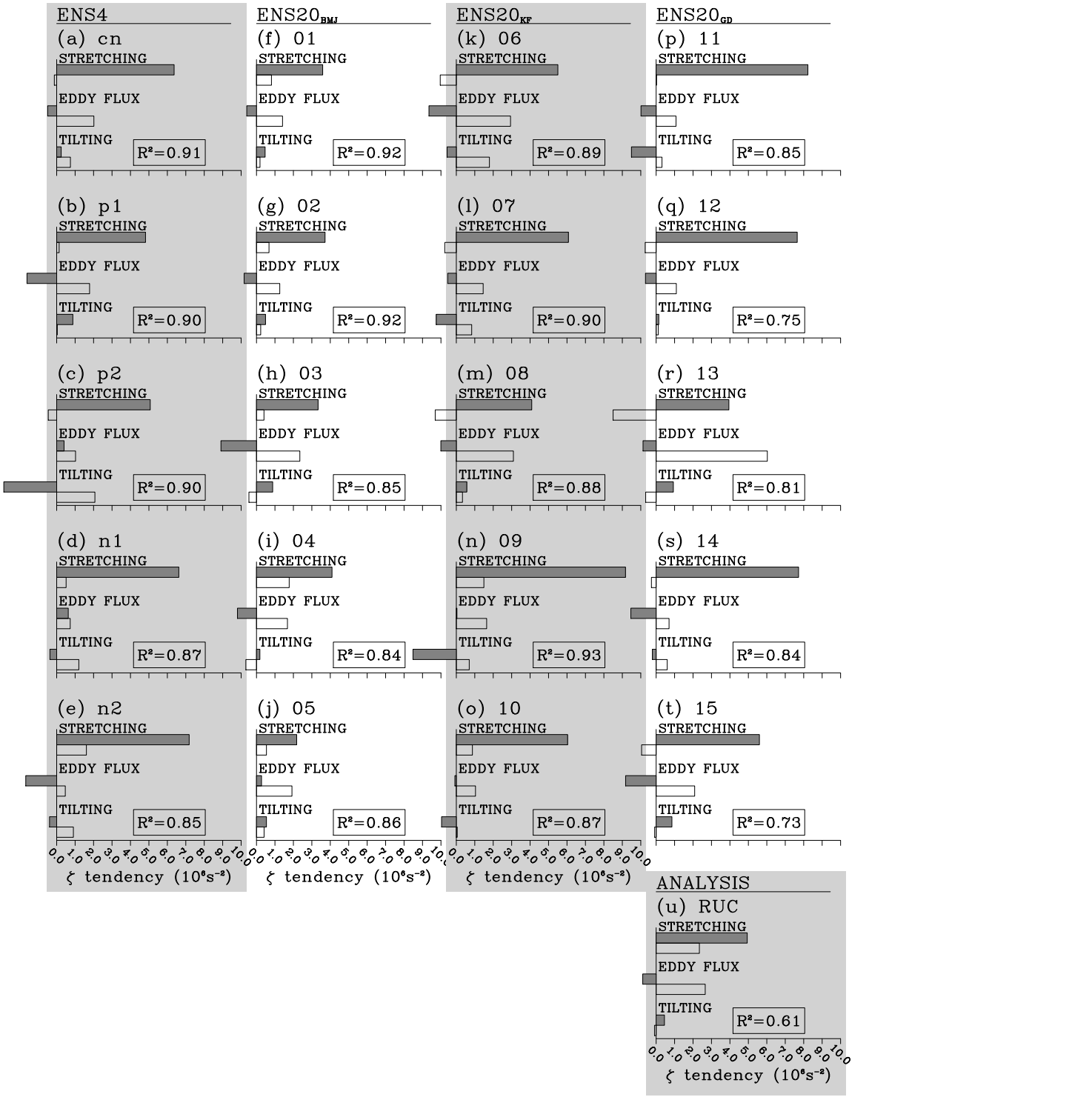

Figure 15 The sum of stretching, eddy flux, and tilting tendency terms for points in time-height space in which the sum of all three tendency terms is positive (gray shaded bars) and negative (black outlined bars) for members in a) – e) ENS4, f) – j) $ENS20_{BMJ}$, k) – o) $ENS20_{KF}$, p) – t) $ENS20_{GD}$, and u) RUC analyses. For the sum of positive (negative) tendencies, the values to the right of zero are positive (negative), so that right of zero always indicates which tendencies contribute most to either positive or negative sums. Spatial correlation coefficients in time-height space between vorticity tendency [LHS of Eq. (3)] and the sum of tendency terms (RHS of Eq. (3)] are indicated at the bottom right of each panel.

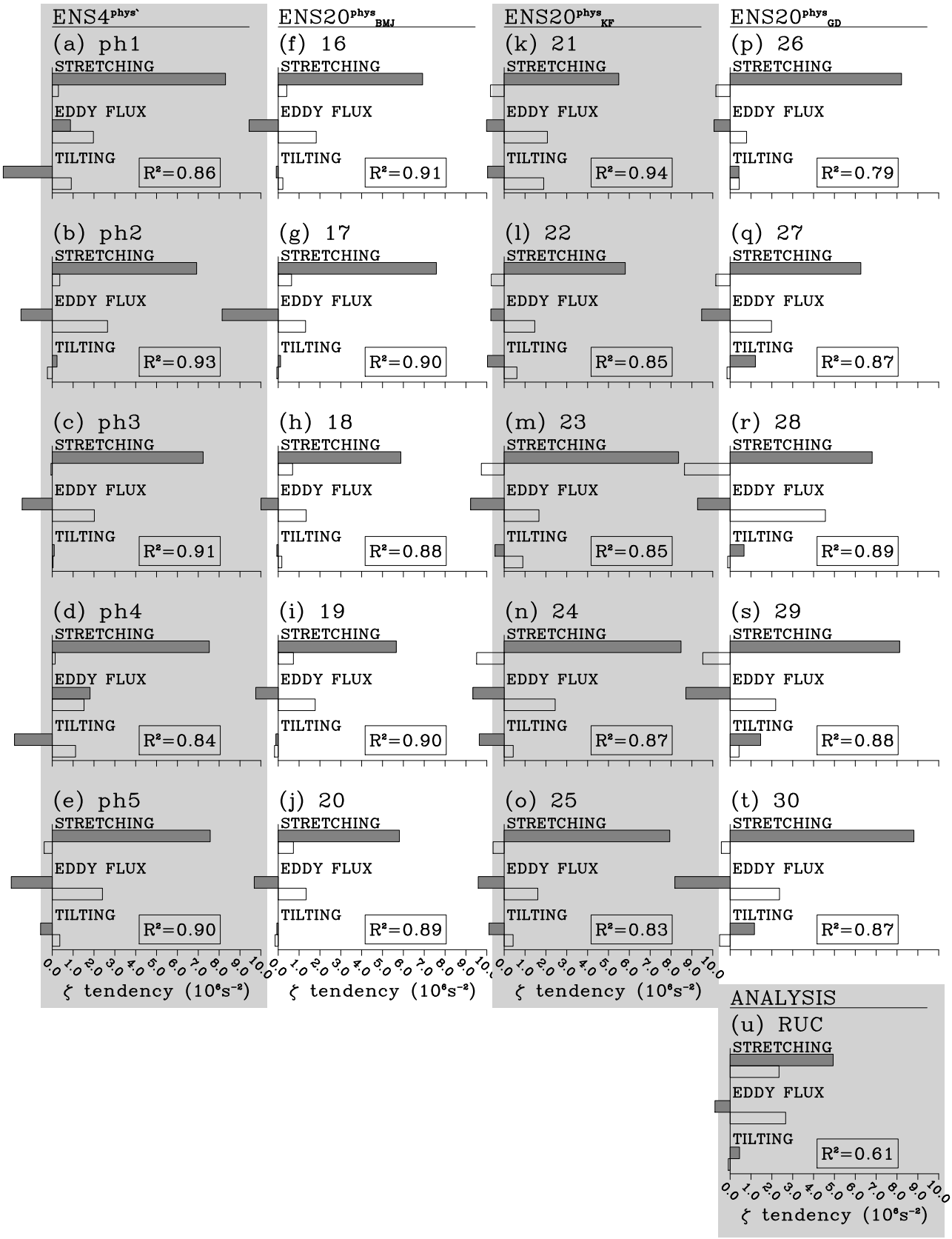

Figure 16 Same as Figure 15 except for a) – e) ENS4^{phys}, f) – j) ENS20$^{phys}_{BMJ}$, k) – o) ENS20$^{phys}_{KF}$, and p) – t) ENS20$^{phys}_{GD}$.

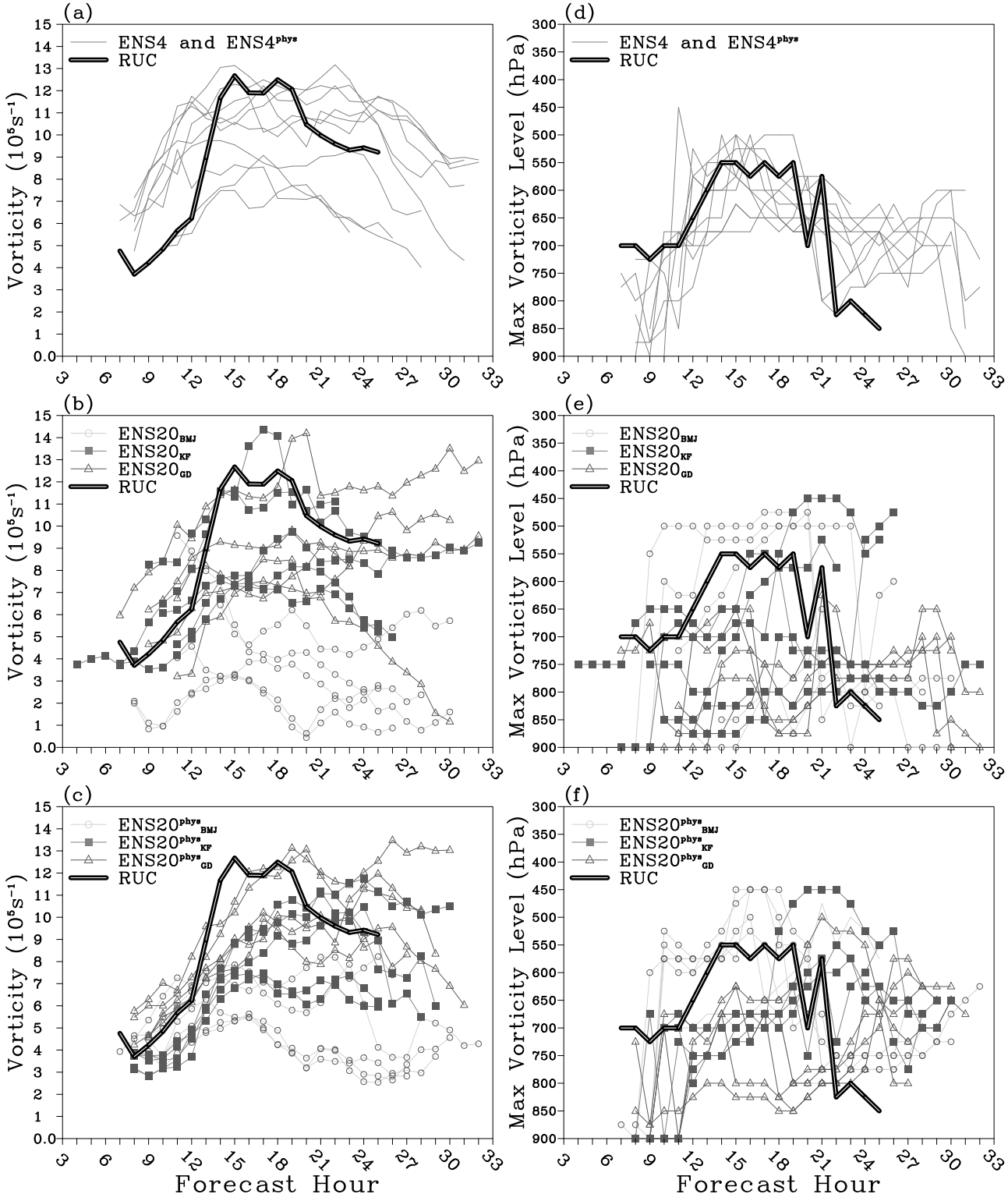

Figure 17 Time series of the maximum vorticity between 900- and 300-hPa for ensemble members in a) ENS4 and ENS4^{phys}, b) ENS20 subsets, and c) ENS20^{phys} subsets, and d) - f) same as a) -c) except for time series of the vertical level at which the maximum vorticity occurred. a) - f) also contain time series from the RUC analysis.

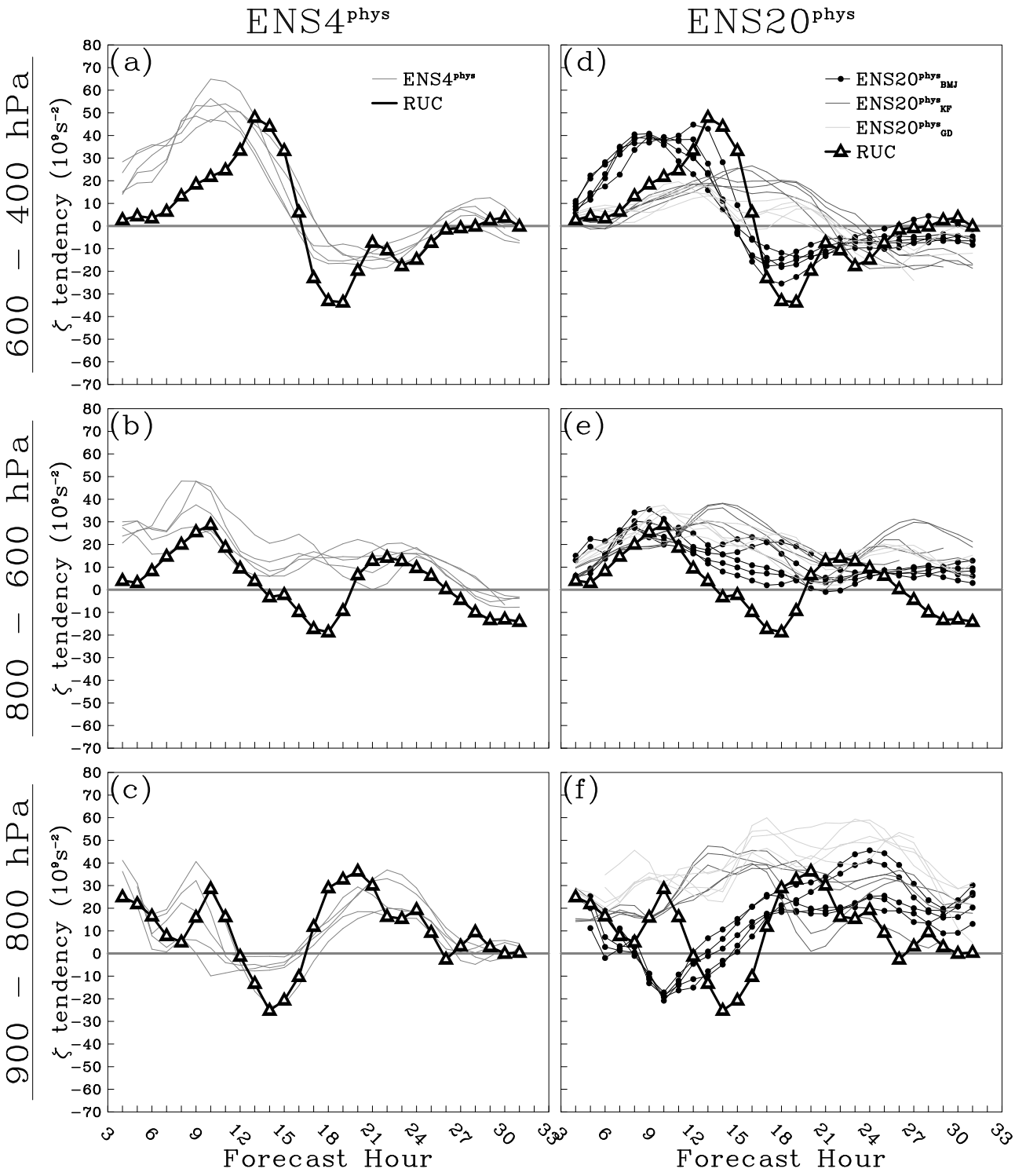

Figure 18 Time series of vortex stretching tendencies in ENS4^{phys} members and RUC analyses averaged over a) 600- to 400-hPa, b) 800- to 600-hPa, and c) 900- to 800-hPa. d) – f) same as a) – c) except for ENS20^{phys} members.

Table 1 ENS4 ensemble member specifications. NAMa and NAMf indicate NAM forecasts and analyses, respectively; em_pert and nmm_pert are perturbations from different SREF members; and em_n1, em_p1, nmm_n1, and nmm_p1 are different SREF members that are used for LBCs. The remaining table elements are described in the text.

Ensemble Member	**ICs**	**LBCs**	**Microphysics Scheme**	**Surface Layer Scheme**	**Boundary Layer Scheme**
CN	21Z NAMa	18z NAMf	WSM-6	Janjic Eta	MYJ
N1	CN - em_pert	21z SREF em_n1	Ferrier	Janjic Eta	MYJ
P1	CN + em_pert	21z SREF em_p1	Thompson	Janjic Eta	MYJ
N2	CN – nmm_pert	21z SREF nmm_n1	Thompson	Monin-Obukhov	YSU
P2	CN + nmm_pert	21z SREF nmm_p1	WSM-6	Monin-Obukhov	YSU

Table 2 Same as Table 1 except for ENS4^{phys} ensemble member specifications.

Ensemble Member	**ICs**	**LBCs**	**Microphysics Scheme**	**Surface Layer Scheme**	**Boundary Layer Scheme**
PH1	21Z NAMa	18Z NAMf	Thompson	Janjic Eta	MYJ
PH2	21Z NAMa	18Z NAMf	Ferrier	Janjic Eta	MYJ
PH3	21Z NAMa	18Z NAMf	WSM-6	Monin-Obukhov	YSU
PH4	21Z NAMa	18Z NAMf	Thompson	Monin-Obukhov	YSU
PH5	21Z NAMa	18Z NAMf	Ferrier	Monin-Obukhov	YSU

Table 3 ENS20 ensemble member specifications. The members are grouped into 5-member subsets that have the same cumulus parameterizations. The ICs/LBCs table elements represent various SREF members and the remaining table elements are described in the text.

Ensemble Member	**ICs/LBCs**	**Cumulus Scheme**	**Microphysics**	**Surface Layer**	**Boundary Layer**
$ENS20_{BMJ}$					
1	em_ctl	BMJ	Thompson	Janjic Eta	MYJ
2	em_p1	BMJ	WSM-6	Janjic Eta	MYJ
3	em_n1	BMJ	WSM-6	Monin-Obukhov	YSU
4	nmm_ctl	BMJ	Thompson	Monin-Obukhov	YSU
5	nmm_p1	BMJ	Ferrier	Monin-Obukhov	YSU
$ENS20_{KF}$					
6	nmm_n1	KF	Thompson	Janjic Eta	MYJ
7	eta_ctl1	KF	WSM-6	Janjic Eta	MYJ
8	eta_n1	KF	WSM-6	Monin-Obukhov	YSU
9	eta_n2	KF	Thompson	Monin-Obukhov	YSU
10	eta_n3	KF	Ferrier	Monin-Obukhov	YSU
$ENS20_{GD}$					
11	eta_n4	Grell-Devenyi	Thompson	Janjic Eta	MYJ
12	eta_p1	Grell-Devenyi	WSM-6	Janjic Eta	MYJ
13	eta_p2	Grell-Devenyi	WSM-6	Monin-Obukhov	YSU
14	eta_p3	Grell-Devenyi	Thompson	Monin-Obukhov	YSU
15	eta_p4	Grell-Devenyi	Ferrier	Monin-Obukhov	YSU

Table 4 Same as Table 3 except for ENS20^{phys} ensemble member specifications.

Ensemble Member	**ICs/LBCs**	**Cumulus Scheme**	**Microphysics**	**Surface Layer**	**Boundary Layer**
ENS20$^{phys}_{BMJ}$					
16	eta_ctl2	BMJ	Thompson	Janjic Eta	MYJ
17	eta_ctl2	BMJ	WSM-6	Janjic Eta	MYJ
18	eta_ctl2	BMJ	WSM-6	Monin-Obukhov	YSU
19	eta_ctl2	BMJ	Thompson	Monin-Obukhov	YSU
20	eta_ctl2	BMJ	Ferrier	Monin-Obukhov	YSU
ENS20$^{phys}_{KF}$					
21	eta_ctl2	KF	Thompson	Janjic Eta	MYJ
22	eta_ctl2	KF	WSM-6	Janjic Eta	MYJ
23	eta_ctl2	KF	WSM-6	Monin-Obukhov	YSU
24	eta_ctl2	KF	Thompson	Monin-Obukhov	YSU
25	eta_ctl2	KF	Ferrier	Monin-Obukhov	YSU
ENS20$^{phys}_{GD}$					
26	eta_ctl2	Grell-Devenyi	Thompson	Janjic Eta	MYJ
27	eta_ctl2	Grell-Devenyi	WSM-6	Janjic Eta	MYJ
28	eta_ctl2	Grell-Devenyi	WSM-6	Monin-Obukhov	YSU
29	eta_ctl2	Grell-Devenyi	Thompson	Monin-Obukhov	YSU
30	eta_ctl2	Grell-Devenyi	Ferrier	Monin-Obukhov	YSU